Journal of Energy Challenges and Mechanics

ISSN 2056-9386

http://www.nscj.co.uk/JECM/

Volume 1, Issue 4
December 2014

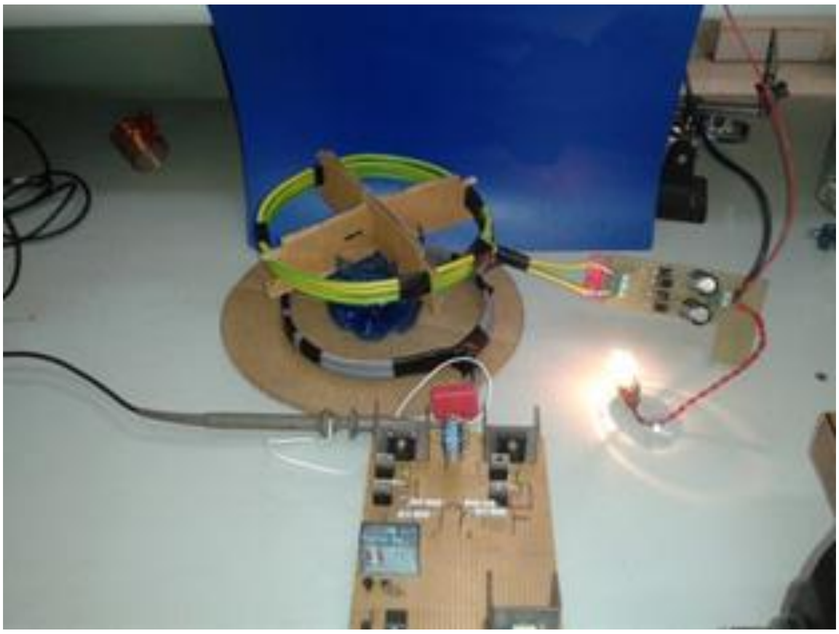

Featured article:

Future energy needs and engineering reality
Michael J Kelly
Electrical Engineering Division, Department of Engineering, University of Cambridge, 9 JJ Thomson Avenue, Cambridge CB3 0FA, UK
Journal of Energy Challenges and Mechanics, volume 1, pages 113-118.

North Sea Conference & Journal LTD
2 Charlestown Walk, Cove Bay, AB12 3EZ, Aberdeen, Scotland, United Kingdom
http://www.nscj.co.uk/JECM/ | jecm@nscj.co.uk | +44(0)1224 875635

Journal of Energy Challenges and Mechanics
http://www.nscj.co.uk/JECM/
ISSN 2056-9386
Volume 1 (2014) issue 4

TABLE OF CONTENTS pages

Journal of Energy Challenges and Mechanics
http://www.nscj.co.uk/JECM/

ISSN 2056-9386
Volume 1 (2014) issue 4, article 1

Biological treatment of effluents generated by amine based CO_2-capture plants

生物处理由胺二氧化碳捕获设备所产生的污水

Ingrid Hauser[1*], Aslak Einbu[2], Hallvard F. Svendsen[3] and Kjetill Østgaard[1]

[1]*Department of Biotechnology, Norwegian University of Science and Technology, Trondheim, Norway*
[2]*SINTEF Materials and Chemistry, Trondheim, Norway*
[3]*Department of Chemical Engineering, Norwegian University of Science and Technology, Trondheim, Norway*

ingrid.hauser@ntnu.no

Accepted for publication on 14th December 2014

Abstract - **Carbon capture and storage (CCS) is a currently developed technology to fight climate change by reducing greenhouse gas emissions from large point sources. There are various capturing principles, whereas to date most of the pilot plants are based on amine absorption. One commonly used primary amine is monoethanolamine (MEA).**

During the process of carbon capture, the solvent is subject to various degradation mechanisms due to oxidation, thermal strain, and unwanted side reactions within the system. After reclaiming the usable solvent for recycling, these degradation products accumulate as waste and need to be treated accordingly. Depending on the solvent, different degradation products may be found in this so called reclaimer waste, with ammonia as a dominant end product. Volatile products may also be emitted through the exhaust gas. Estimates from a full-scale amine-based capture plant predicts approximately 0.2 ppm amine and 20 ppm ammonia in the emissions. For a full-scale capture plant removing 1 million tons CO_2 annually, these concentrations implicate emissions of significant environmental impact.

Effluents from those various sources within the capture plant can be treated biologically to obtain nitrogen removal as well as general detoxification. Our studies have shown that MEA, as well as MEA-based reclaimer waste, can be treated with biological nitrogen removal, which is a well-established method within the field of wastewater treatment. Most important, by applying a recycled pre-denitrification reactor configuration, we have shown that the amine and its organic degradation products will serve efficiently as the carbon source needed for the denitrification step. Future development has to take these findings into consideration.

Keywords – **Biodegradation; Carbon capture and storage; Monoethanolamine; Nitrification**

I. INTRODUCTION

Carbon capture and storage (CCS) has received much attention in the recent years. It is thought that with CCS, the global CO_2 emission can be reduced until society is technologically as well as morally ready to shift from fossil fuel to alternative energy sources. In fact, the public acceptance of CCS depends on a variety of factors, such as the type of information, religious faith and others [1, 2]. However, to date many knowledge gaps of the technological side need to be filled before CCS can be employed at a large scale.

CCS relies on various capture mechanisms, whereas amine based post combustion CO_2-capture has been tested on more than 25 pilot plants, approaching full scale application on coal-fired plants [3]. One reason why carbon capturing from large point sources is not yet commercially viable is that such a large scale application of solvent has to carefully consider essential environmental aspects such as solvent emissions or spillage, as well as waste handling [4-9]. It is not only the solvent itself, but also various degradation products that have to be included in the assessment. The solvents used in the CCS process need to meet many criteria. For example, the solvent needs to have good thermodynamic and mass transfer properties and be stable at process conditions, while at the same time being easily degradable in the environment [10]. Monoethanolamine (MEA) is an example of a well-studied alkanolamine, as it has been applied for decades in the gas sweetening industry and also found application in CCS [11].

II. SOURCES OF WASTE IN CCS

During the process of carbon capture, the solvent reacts with components of the flue gas. In general, the solvent is also subject to oxidative as well as thermal degradation. In flue gas coming from a fossil fuel-fired boiler there are CO_2, O_2, CO, SO_x, NO_x, fly ash, and other impurities, which make it very complex to predict all side reactions [12]. Therefore, waste effluents of CCS may include compounds in the liquid as well as in the gas phase. During CCS operation, a slip stream from the stripper column is taken and the degraded solution containing high molecular weight compounds and heat stable salts is separated via distillation from the useful amine [13], see Fig. 1. This so called 'reclaimer waste' contains mainly amine, ammonia, heat stable salts and other degradation products. The actual composition will depend on the type of solvent, process conditions, and flue gas quality. According to recent literature the generated amount of this type of waste ranges from 1.17kg/ton CO_2 to 3.94kg/ton CO_2 depending on flue gas composition and operational conditions [9].

Another source of waste produced in CCS is the exhaust gas. To avoid unwanted emissions of volatile amines or degradation products to the environment, the exhaust gas goes through multiple water washes. These water wash sections will remove ammonia from the gas, but over time they become saturated. Therefore, the circulating water needs to be exchanged and treated.

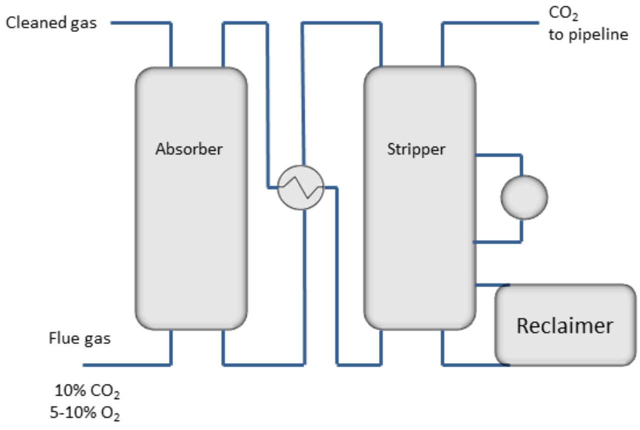

Fig. 1 Process flow diagram of typical post-combustion CO_2 capture by amine absorption, adapted from [13] .

Maximum atmospheric emissions from simulations of a coal fired MEA based capture plant are reported with 5.5 and 1.14 mg/Nm^3 (dry CO_2 lean Flue gas) for MEA and NH_3, respectively [14]. Other reported volatile compounds are diethanolamine (DEA), formaldehyde, acetaldehyde, acetone, methylamine and acetamide [14].

III. Biological Nitrogen Removal

Biological nitrogen removal is based on the sequential reduction of ammonia to inert nitrogen. It is a key process in the natural nitrogen cycle and has been applied for wastewater treatment during the last century. This two-step process can be divided into nitrification and denitrification. The first step comprises the oxidation of ammonia to nitrate via nitrite and is facilitated by two groups of bacteria, namely the ammonia oxidizing bacteria (AOB) and the nitrite oxidizing bacteria (NOB), in two steps (Eqs. (1) and (2)):

$$NH_4{}^+ + \tfrac{3}{2}O_2 \rightarrow NO_2{}^- + H_2O + 2\,H^+ \tag{1}$$

$$NO_2{}^- + \tfrac{1}{2}O_2 \rightarrow NO_3{}^- \tag{2}$$

Commonly expressed by the total sum (Eq. (3)):

$$NH_4{}^+ + 2\,O_2 \rightarrow NO_3{}^- + H_2O + 2\,H^+ \tag{3}$$

Both of these phylogenetically unrelated bacteria groups are chemolithoautotrophic, meaning they use inorganic compounds such as NH_4^+ and nitrite as energy source while utilizing carbon dioxide as the carbon source. Due to the low energy yield, they grow very slow compared to the denitrifying bacteria in the following step.

In the next step, the generated nitrate is stepwise reduced to molecular nitrogen by denitrifying bacteria, as shown in Eq. (4).

$$Organic\ matter + NO_3{}^- + H^+ \rightarrow N_2 + CO_2 + H_2O \tag{4}$$

In the absence of oxygen, some bacteria may use nitrate as the terminal electron acceptor for respiration instead of oxygen. Most denitrifying bacteria are facultative, meaning they can switch their respiration from oxygen to nitrate. Denitrification occurs then only under severe oxygen limiting conditions, because oxygen is energetically more favorable than nitrate [15].

Denitrifying bacteria are heterotroph, meaning they need organic carbon for energy metabolism, as well as for growth. The denitrifying bacteria belong taxonomically to various subclasses of the *Proteobacteria*. However, the ability to denitrify can also be found among archeae and core enzymes have even been found in fungi [15].

IV. Biodegradation

Many natural occurring compounds have a functional role in at least one or more microbial metabolic pathways. This means that bacteria utilize them as a carbon source, or in their energy metabolism. Xenobiotics are man-made compounds, which do not occur naturally. However, many of these compounds may also be utilized by microbes if they can be made available to the bacteria and the conditions are right.

The persistency of a compound will depend on the chemical structure, the concentration and the environmental conditions for degradation. Monoethanolamine (MEA) is an easily degradable alkanolamine, but at high concentrations it was shown to persist for decades in soil [16]. Another aspect to consider when treating undefined mixed waste is that certain compounds might act synergistic or antagonistic in combination [17].

In general, biodegradation depends on chemical reactions catalyzed by extra- and intra-cellular enzymes. Larger molecules are hydrolyzed to smaller compounds before cellular uptake and the final oxidation to carbon dioxide. In the absence of an external electron acceptor, reduced products such as methane will accumulate. Thus, MEA based reclaimer waste has been successfully degraded even under anaerobic conditions for biogas production [18-21].

A common measure for the biodegradability of a compound is the so called biological oxygen demand (BOD). During this test the microbial aerobic degradation of a compound is determined by measuring the oxygen consumption during degradation over a set time frame, such as 7 days in the standardized OECD Test No. 301 [22]. For solvents used in CCS, a lot of work has been invested to test the biodegradability of amines in seawater [23], whereas data on freshwater is yet scarce. We are currently testing amine biodegradability in freshwater with both oxygen and nitrate as alternative electron acceptors for oxidation.

V. PROCESS CONSIDERATIONS

For biological nitrogen removal there are multiple alternative process solutions available. The post- and pre-denitrification set-up illustrated in Fig. 2 have recently been tested for treatment of MEA [24]. A post-denitrification set-up is beneficial if the influent contains ammonia and only low amounts of organic matter. The aerated nitrifying reactor will convert ammonia to nitrate that serves as an electron acceptor in the second denitrifying step. Amine waste contains substantial amounts of ammonia, but also vast amounts of organic matter.

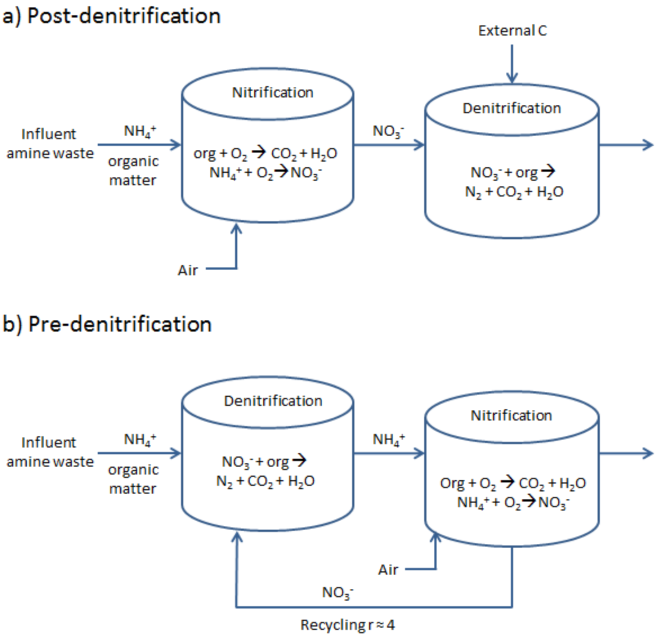

Fig. 2 Alternative process configurations.

This may be utilized aerobic by heterotrophic competing with the nitrifyers for oxygen, thus decreasing the nitrification efficiency. In an open system, autotrophic nitrifying bacteria are always accompanied by heterotrophic bacteria, and their competition for space and oxygen is a well-known phenomenon, particularly in biofilm systems [25]. For the nitrogen removal efficiency this does not have to play a major role, but in terms of economy, the additional feed of organic matter in the following denitrifying step may be of significance.

The obvious solution is to feed the heterotrophic denitrifying bacteria with the available organic matter in the amine waste. This can be achieved with the pre-denitrification set-up where the amine waste reaches the anoxic denitrification reactor first, see Fig. 2b. Here the amine can be biodegraded, resulting in ammonia and other organic compounds. The organic matter represented by the amine itself serves as a carbon source, while the bulk fraction of ammonia continues into the aerated nitrifying reactor (Fig. 2b). Ammonia will there be biologically oxidized to nitrate, which then has to be recycled to the denitrifying bacteria, to serve as the electron acceptor for their respiration. One disadvantage of this set-up may be that there will always be some nitrate lost in the effluent. However, the cost saving advantage of not needing any additional carbon source is the most important factor. We have recently successfully treated MEA as well as real reclaimer waste from an amine based CO_2-capture plant with this set-up [24, 26].

Another crucial factor in bioprocess engineering is the retention of the biocatalyst in a continuous flow. Losses have to be minimized so that bacterial growth can compensate to maintain a steady state activity. This is of particular importance for the slow-growing nitrifiers, with a doubling time of 1 day or more. We have applied so called moving bed biofilm carriers to achieve successful retention and activities [24, 26].

The corresponding diffusion transport dominated micro-environment of the biofilm has been found to determine the actual organic loading capacity as well as toxic inhibition of such as system, work is in progress to understand and model those essential process parameters in detail.

VI. NEW SOLVENTS

Developing new capture solvents is currently an ongoing research topic [27]. As mentioned above, the solvent must show stability during process conditions, as well as be easily degradable in the environment. According to Hoff et al. [10] most of the first generation post combustion solvents belong to one of the following groups: Two- component buffer plus promoter systems (activated AMP or MDEA), single component amine system with high molecular efficiency (MEA, Piperazine), amino acid systems using strong base or amine as neutralizing agent (KOH + Glycine), or promoted carbonates (K_2CO_3 + activator) [10]. All of these solvent groups show more or less chemical degradation during process condition. Volatility is another important aspect. Amino acids show low volatility [10], and in terms of biodegradability in marine environment, amino acids show low toxicity and high biodegradability. However, tertiary amines, compounds containing quaternary carbons and some solvents (such as AMP and MDEA) did not degrade easily in sea water [23]. Researchers are currently working on third generation solvents, aiming on improving their energy efficiency.

VII. CONCLUSION

Biodegradability tests of solvents need to be applied before large scale utilization in CCS can be done. For many solvents data exist, but not for all relevant environments. A limitation of the BOD testing is that just the aerobic degradation is determined and not the anoxic degradability which is crucial in biological waste treatment as illustrated.

Efficient waste and effluent treatment must be integrated in the evaluation and choice of future solvent systems. We have shown how this can be tested in lab scale to develop suitable compact bioprocess plants for this purpose [24, 26].

REFERENCES

[1] A. L. B. Hope and C. R. Jones. "The impact of religious faith on attitudes to environmental issues and Carbon Capture and Storage (CCS) technologies: A mixed methods study," *Technology in Society,* **38**, pp. 48-59, 2014.

[2] C. Oltra, R. Sala, and À. Boso. "The influence of information on individuals' reactions to CCS technologies: results from experimental online survey research," *Greenhouse Gases: Science and Technology,* **2**, pp. 209-215, 2012.

[3] M. E. Boot-Handford, J. C. Abanades, E. J. Anthony, M. J. Blunt, S. Brandani, N. Mac Dowell, *et al.* "Carbon capture and storage update," *Energy & Environmental Science,* **7**, pp. 130-189, 2014.

[4] A. J. Reynolds, T. V. Verheyen, S. B. Adeloju, E. Meuleman, and P. Feron. "Towards Commercial Scale Postcombustion Capture of CO2 with Monoethanolamine Solvent: Key Considerations for Solvent Management and Environmental Impacts," *Environmental Science & Technology,* **46**, pp. 3643-3654, 2012.

[5] E. S. Rubin, H. Mantripragada, A. Marks, P. Versteeg, and J. Kitchin. "The outlook for improved carbon capture technology," *Progress in Energy and Combustion Science,* **38**, pp. 630-671, 2012.

[6] B. Singh, A. H. Strømman, and E. G. Hertwich. "Environmental Damage Assessment of Carbon Capture and Storage," *Journal of Industrial Ecology,* **16**, pp. 407-419, 2012.

[7] K. Veltman, B. Singh, and E. G. Hertwich. "Human and Environmental Impact Assessment of Postcombustion CO2 Capture Focusing on Emissions from Amine-Based Scrubbing Solvents to Air," *Environmental Science & Technology,* **44**, pp. 1496-1502, 2010.

[8] P. Zapp, A. Schreiber, J. Marx, M. Haines, J.-F. Hake, and J. Gale. "Overall environmental impacts of CCS technologies—A life cycle approach," *International Journal of Greenhouse Gas Control,* **8**, pp. 12-21, 2012.

[9] L. Nurrokhmah, T. Mezher, and M. R. M. Abu-Zahra. "Evaluation of Handling and Reuse Approaches for the Waste Generated from MEA-based CO2 Capture with the Consideration of Regulations in the UAE," *Environmental Science & Technology,* **47**, pp. 13644-13651, 2013.

[10] K. A. Hoff, E. F. d. Silva, I. Kim, A. Grimstvedt, and S. Ma'mun. "Solvent development in post combustion CO2 capture-Selection criteria and optimization of solvent performance, cost and environmental impact," *Energy Procedia,* **37**, pp. 292-299, 2013.

[11] K. Ohtaguchi, K. Koide, and T. Yokoyama. "An ecotechnology-integrated MEA process for CO2-removal," *Energy Conversion and Management,* **36**, pp. 401-404, 1995.

[12] B. R. Strazisar, R. R. Anderson, and C. M. White. "Degradation Pathways for Monoethanolamine in a CO2 Capture Facility," *Energy & Fuels,* **17**, pp. 1034-1039, 2003.

[13] G. S. Goff and G. T. Rochelle. "Monoethanolamine Degradation: O2 Mass Transfer Effects under CO2 Capture Conditions," *Industrial and Engineering Chemistry Research,* **43**, pp. 6400-6408, 2004.

[14] IEAGHG, "Gaseous emissions from amine based PCC processes and their deep removal," May, 2012.

[15] W. G. Zumft. "Cell biology and molecular basis of denitrification," *Microbiology and Molecular Biology Reviews,* **61**, pp. 533-616, 1997.

[16] A. W. Ndegwa, R. C. K. Wong, A. Chu, L. R. Bentley, and S. R. D. Lunn. "Degradation of monoethanolamine in soil," *Journal of Environmental Engineering and Science,* **3**, pp. 137-145, 2004.

[17] A. Leuchtenberger, *Grundwissen zur mikrobiellen Biotechnologie*: Springer, 1998.

[18] S. Wang, J. Hovland, and R. Bakke. "Efficiency of the anaerobic digestion of amine wastes," *Biotechnology Letters,* **35**, pp. 2051-2060, 2013.

[19] S. Wang, J. Hovland, and R. Bakke. "Anaerobic degradation of carbon capture reclaimer MEA waste," *Water Science and Technology,* **67**, pp. 2549-2559, 2013.

[20] S. Wang, J. Hovland, and R. Bakke. "Modeling and simulation of lab-scale anaerobic co-digestion of MEA waste," *Modeling, Identification and Control,* **35**, pp. 31-41, 2014.

[21] S. Wang, J. Hovland, S. Brooks, and R. Bakke. "Detoxifying CO2 Capture Reclaimer Waste by

Anaerobic Digestion," *Applied Biochemistry and Biotechnology*, pp. 1-8, 2013.

[22] OECD, *Test No. 301: Ready Biodegradability*: OECD Publishing.

[23] I. Eide-Haugmo, O. G. Brakstad, K. A. Hoff, K. R. Sørheim, E. F. da Silva, and H. F. Svendsen. "Environmental impact of amines," *Energy Procedia*, **1**, pp. 1297-1304, 2009.

[24] I. Hauser, A. Colaço, J. Skjæran, A. Einbu, K. Østgaard, H. Svendsen, *et al.* "Biological N Removal from Wastes Generated from Amine-Based CO2 Capture: Case Monoethanolamine," *Applied Biochemistry and Biotechnology*, **169**, pp. 1449-1458, 2013.

[25] A. Ohashi, D. G. Viraj de Silva, B. Mobarry, J. A. Manem, D. A. Stahl, and B. E. Rittmann. "Influence of substrate C/N ratio on the structure of multi-species biofilms consisting of nitrifiers and heterotrophs," *Water Science and Technology*, **32**, pp. 75-84, 1995.

[26] I. Hauser, A. Einbu, K. Østgaard, H. Svendsen, and F. Cervantes. "Biodegradation of amine waste generated from post-combustion CO2 capture in a moving bed biofilm treatment system," *Biotechnology Letters*, **35**, pp. 219-224, 2013.

[27] M. R. Abu-Zahra, Z. Abbas, P. Singh, and P. Feron, "Carbon Dioxide Post-Combustion Capture: Solvent Technologies Overview, Status and Future Directions," in *Materials and processes for energy: communicating current research and technological developments* A. Mendez-Vilas, Ed., ed Badajoz: Formatex Research Center, 2013.

Journal of Energy Challenges
and Mechanics
http://www.nscj.co.uk/JECM/

ISSN 2056-9386
Volume 1 (2014) issue 4, article 2

Wireless Power Transmission Technology for Contactless Recharging and Batteryless Supply

无线电力传输技术用于非接触充电和无电池供应

Leopoldo Angrisani, Guido d'Alessandro, Massimo D'Apuzzo, Mauro D'Arco*

Department of Electrical and Information Technology Engineering, University of Naples Federico II, Naples, 80125, ITALY

mauro.darco@unina.it

Accepted for publication on 22th July 2014

Abstract – **During the last years, three main approaches to transmit power without cable connections have been studied. The first one relies on microwave radiating systems, and its performance is mostly limited by the rectenna device, required to pick-up and DC convert the radiated power. This approach has not pervaded application fields since its hazardousness is still not well assessed. Moreover, it has still to face several technological issues and safety concerns before being eligible for application. The second one refers to optical wireless transmission at long distances, which uses laser and photovoltaic diodes for successful operation. The third approach exploits coupled circuits to transmit power upon short or midrange distances. Its breakthrough is gaining attention in a number of application fields, such as radiofrequency identification, small batteryless home appliances, mobile devices and electrical vehicles recharging, wireless and body sensor networks.**

The paper deals with wireless power transmission technology based on the third approach, and takes into account two classes of applications: contactless recharging and batteryless supply. Contactless recharging involves the possibility of keeping an electrical equipment, and specifically its internal battery, grid disconnected, without giving up to its recharging. Batteryless supply permits the functioning of remote wireless equipment, often deployed in networked architectures, which are more and more valued for their fast installation and easy re-positioning features. For both classes, the benefits that can be achieved by adopting wireless power transmission are also highlighted.

An experimental study is finally carried out. To this end, a typical architecture of a power transmission system relying on resonance-based coupling mechanisms is implemented. The ground electronics of the simple set-up, which uses a relaxation oscillator in the primary circuit and a full-rectifier bridge in the secondary to attain DC power, is described in detail. The obtained results show the efficiency of the power transfer mechanism both for nominal operative conditions and different ones characterized by deliberate mismatches.

Keywords – **Wireless power transmission, Contactless recharging, Batteryless supply, resonance-based coupling.**

I. INTRODUCTION

The idea of wireless power transmission (WPT) dates back to the age of the popular scientist and inventor Nikola Tesla (Smiljan, 1856 – New York, 1943) [1]. This innovative idea was judged visionary at that time, while it has been reconsidered by the scientific community in the last decades. In fact, in the mid '60, pioneering experiments aimed at supplying a light helicopter by means of an electrical source on the ground were successfully carried out [2]. In particular, a microwave link between a power source, consisting of a magnetron connected to a parabolic antenna, and a receiving antenna was set-up: the parabolic antenna granted the focalization of the radiated energy into a collimated beam, while the receiving antenna (rectenna), positioned on-board the helicopter, converted the microwave energy into DC power by means of surface-integrated rectifier diodes [3]. Several other similar experiments followed during the late '60 and all along the '70 attest the extensive efforts to improve the performance of the rectenna. The vacuum tubes were substituted with semiconductor and Schottky diodes, and thin-film technologies, which allowed to realize surface-mounting rectennas characterized by reduced size and weight, were also introduced. However, despite the considerable amount of research and development actions produced in the last decades, the microwave WPT technology has not pervaded relevant application fields.

Optical WPT at long wavelengths technology has been proposed as an alternative. This uses lasers diodes to convert electrical power to a collimated beam at the source side and photovoltaic diodes to retrieve electrical power at the receiving side. Unfortunately, Optical WPT has still to face several technological issues and safety concerns before being eligible for applicative scenarios, hence, as for the microwave WPT technology, at present, its applications are at an experimental stage.

At the contrary, wireless power transmission breakthrough has occurred in applications that use radiofrequency or even lower frequency to transmit energy without cables, often by means of resonant coupled circuits [4]-[7]. The most relevant examples are radio frequency identification (RFID) [8], mobile devices and electrical vehicles recharging [9], battery-less equipment supply, body sensor networks (BSN) deployment, and implantable microelectronic devices, such as cochlear and retinal implants.

In this paper, both contactless recharging and battery-less supply topics are dealt with. Contactless induction mechanisms represent a valuable solution to recharge battery powered vehicles when plugging to the mains reveals troublesome or impossible [10]. Batteryless devices are attractive both from a pragmatic point of view, because of the strategic role they can play in critical logistic scenarios, and from an innovation-oriented point of view, because of the novelty that WPT technology can add to new groundbreaking remote equipment pursuit. In fact, the battery supply is often recognized as a critical aspect of remote equipment functioning, being the periodical battery replacement non-strategic and, sometimes, problematic.

II. CONTACTLESS RECHARGING

Technologies enabling contactless recharge of equipment have been studied for long time and several different solutions have been proposed and developed. A contactless power transfer system permits to avoid the problems that arise when power transmission, such as that required for battery recharging, has to be realized without electrical plugging, or any other locked connection to the energy source. To this end systems exploiting coupled circuits to transmit power within very short distances are typically considered. The coupling is made possible by means of two separated coils at the front-end of a primary and a secondary circuit. The primary coil is energized to produce an induction flow that is concatenated by the secondary coil. At the terminals of the secondary coil the necessary power to recharge the batteries is retrieved from the primary circuit thanks to the coupling mechanism.

The ground electronic is typically designed in order to let the primary circuit evolve according to its own oscillatory mode after having been energized. Such a free-oscillator architecture shows a main advantage with respect to systems in which the primary circuit is driven by a controller, being it capable of continually auto-tuning to the resonant frequency of the system, and thus, of avoiding energy losses caused by changes of the circuit parameters and surrounding environment. At the state of art, this is the most common solution to achieve sufficient power transmission efficiency, which is a key indicator to evaluate the performance of any proposal.

It is worth noting that a relevant contribution to contactless recharging has come from the sector of robotic vehicles, in which vehicles capable of navigating to a recharge station, as soon as low battery is signaled, have been investigated. Specifically, for various applications, vehicles have to be capable of autonomously connecting to the recharging station and waiting until the recharge is fulfilled [11]. This task is highly critical especially for light vehicles, such as unmanned aerial vehicles (UAV), which try to autonomously recharge by landing on auxiliary mobile platforms at ground [12]. Often UAVs undergo fails at recharging because of the difficulties at connecting to the platform, since the vehicles must land in a precise position on the platform to have their own pins in electrical contact to the terminals of the battery recharger.

III. BATTERYLESS SUPPLY

In the recent years batteries technology has become a hot topic that has seen relevant investments and efforts aimed at realizing and delivering long-lasting batteries in order to reduce the replacement frequency. The main efforts in this field have concerned the definition and implementation of energy/power management approaches to be integrated in smart battery systems, similar to those employed in portable computers. Smart batteries include an on-board microcontroller, the firmware of which consists in algorithms that successfully allow to avoid energy misuse at the expense of increased complexity and costs.

Anyway, despite noteworthy advancements have been achieved, at present, the use of embedded batteries is still definitively discouraged in some applications. Generally, this is the case of monitoring applications that use sensors that have to be sealed in plastic enclosures, which limit or make even risky maintenance operations, or that are installed in difficult to reach sites, that make expensive or difficult battery replacement. Also, the case of military applications, in which an ancillary battery-supplied sensor is utilized exclusively to perform periodically checks of the status of a main battery, can be considered. Here the main battery is necessary to power-on weapons that are typically deployed in critical logistic scenarios, where electricity provision is unavailable or unreliable, or that are grid-disconnected for safety even if plugs to the grid are at easy disposal. The ancillary sensors are sometimes supplied by the same battery that assists the weapons: their role is of utmost importance, since a fail of them in signaling a low level battery state would lead to a situation in which the weapons could unexpectedly be unusable.

Nonetheless, the use of batteries is connected to environmental issues, which represent a further reason to discourage battery exploitation. Used batteries are special wastes that have to be properly treated in order to perform recycling and reduce their environmental impact.

Recently, wireless sensor networks harvested by ambient energy (WSN-HEAP) have also been proposed. The underneath technology, at the state-of-art, is utilized in systems characterized by low power consumption. These typically deploy an extra back-up battery to support power peaks or intervene in case of any other power unavailability, thus granting the regular operation. But, back-up batteries suffer of deterioration, require cyclic checks, and need occasionally replacements; therefore, HEAP technologies do not represent a definite solution to the aforementioned problems.

WPT technology can be considered a viable solution to avoid the use of batteries in systems for which plugging to the grid is not convenient. As for contactless recharging applications resonant-based WPT systems can supply remote equipment by exploiting the magnetic coupling between a set of conductive coils. Several interesting experiments show that remote equipment such as sensors can reliably operate without batteries for collecting and transmitting measurement data to a central collector.

IV. RESONANT COUPLED CIRCUITS

For both contactless recharging and batteryless supply an inductive coupling can be exploited to perform wireless power transmission satisfying a wide range of power requirements. In detail, induction systems rely on the magnetic component of a quasi-evanescent but not radiating field. In fact, the induction mechanism is the prevalent magnetic phenomenon observed in the presence of low frequency field variations, whereas it becomes very feeble at radio frequencies [13].

The coupling is usually realized by means of coils, loops or windings. The operating frequencies can be between 10 kHz and 1 MHz, which are typical of circuits including coil inductors. The distance at which the power can be transmitted is a function of several parameters, some of which are related to the geometry, mutual position, and consistency of the coils (radius, mutual distance, alignment, number of turns), others depend on the circuitry parameters such as inductance and capacitance values.

The power transmission actually occurs when a load is connected to the terminals of the coil to form a closed secondary circuit. The transmitted power could include both an active and a reactive component even if the load is a mere resistor. The convenience for a resonance condition can be thus also explained, observing that, to obtain the maximum power transfer, the secondary circuit has to be arranged in order to annul the whole reactance or susceptance. To this end the series or parallel insertion of a capacitor between the coil and the load shows to be effective. It can be shown that series insertion allows to annul the reactance of the secondary circuit; it is thus suggested to feed high impedance loads working with low level currents. Parallel configurations annul the susceptance of the circuit and are suitable to feed low resistance loads working with high currents.

In several applications, especially when the coils are not immobilized, the auto and mutual inductance parameters can change. In these cases, it is necessary to implement suitable control strategies to preserve efficiency in the power transfer.

The most commonly adopted solutions avoid the implementation of control strategies by deploying a relaxation oscillator in the primary circuit [14]-[16]. These types of oscillators are capable of continually auto-tuning the frequency of the system in order to maximize the power transfer efficiency without neither requiring active driving of the frequency nor variable capacitors in the secondary circuit. For other solutions in which the primary circuit is driven by a sinusoidal current source, any tuning mismatch of the secondary circuit would lead to efficiency losses in the power transfer.

In the next Section a typical system architecture, based on the use of a Royer oscillator is considered [17]-[19]. The circuit is directly introduced throughout a description and its functioning is described by means of simulations.

For these applications an empirical design is usually preferred by engineers, since theoretical approaches aimed at estimating the power transmission efficiency, such as the couple-mode theory or reflected load theory (RLT), show some drawbacks. In particular CMT is only applicable to coils with high quality factors and large coupling distance, while an analysis by RLT can be rather delicate.

V. TYPICAL SYSTEM ARCHITECTURE

A typical system architecture includes a primary circuit which is magnetically coupled to a secondary one to be remotely energized. The primary circuit is essentially a relaxation oscillator made up of a resonant tank, realized connecting a capacitor Cr and a centered-tapped coil Lr.

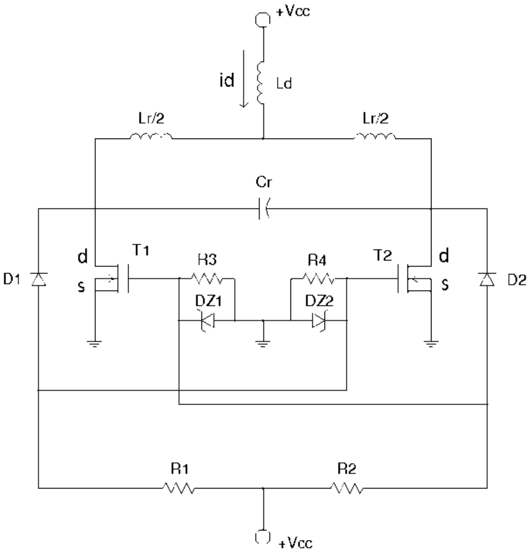

Fig.1, Schematic of a Royer oscillator made up of two identical conducting branches, each one consisting of a MOSFET transistor, a diode and a resistor.

The secondary circuit has a front-end made up of a second coil connected to a capacitor to form an identical resonant tank.

To illustrate in details the functioning of such a system, a very simplified schematic of the primary circuit is given in

Fig. 1. The circuit is made up of two identical conducting branches, each one consisting of a MOSFET transistor, a diode and a resistor, i.e. R1=R2, R3=R4, D1=D2, DZ1=DZ2, and T1=T2. The layout does not show the snubber circuits necessary for power MOSFETs protection during switching on and off transients.

In branch number 1, the current is withdrawn by the DC supply, Vcc, through resistor R1, and flows towards ground either through the diode D1 and the cascaded transistor T1, if transistor T1 is switched-on, or else through Zener diode DZ2. Equally, in branch number 2, the current is withdrawn by the same supply through resistor R2 and goes to ground either through diode D2 and the cascaded transistor T2, if transistor T2 is switched-on, or through Zener diode DZ1.

It is worth noting that, at turn on, being the circuit symmetrical, there should be no voltage difference between the terminals of the resonant LrCr tank connected to the transistors drains. But, in the practice the weak asymmetries and background noise in the tank start progressively mounting current and voltages oscillations. The asymmetries and noise act in conjunction with a positive reaction, obtained by cross-connecting the gate terminal of each transistor to the anode terminal of the diode that probes the conducting state of the other transistor in the opposite branch.

To help the injection and sustainment of the oscillations in the tank, a supplementary path for the current is arranged in the circuit by linking through a choke inductor the central tap that separates the two halves of the Lr coil to the DC supply. To limit the peak currents the inductance of the choke is chosen much greater than that of the coil forming the resonant tank.

At steady state the transistors work in push-pull mode by switching on and off upon the polarity alternation of the sinusoidal voltage across the capacitor Cr.

The circuit functioning can be simulated for several different configurations. As an example, for a configuration characterized by R1=R2=33 Ω, R3=R4=10 kΩ, Ld=1 mH, Lr=1 µH, Cr=350 nF, the current waveforms in the transistor T1, Zener diode DZ1, and inductor Lr evolve to the steady state conditions illustrated in Fig.2.

VI. MEASUREMENT RESULTS

A prototype of the power transmission system described in the previous section has been realized to conduct an experimental study. The prototype utilizes a couple of twin coils made up of five circular copper windings and characterized by a diameter equal to 14 cm.

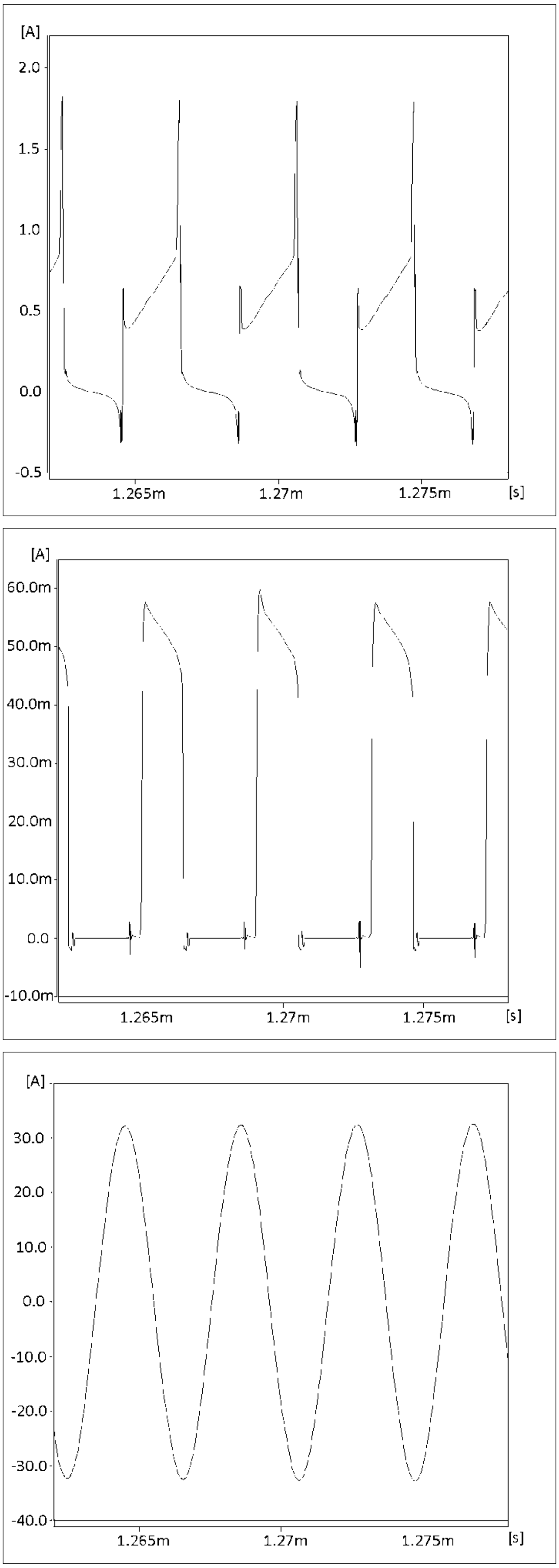

Fig.2, From top to bottom, the current waveforms for: MOSFET transistor T1, Zener diode D1, and inductor Lr.

For test purposes a measuring station consisting of a power supply, multimeters, a digital oscilloscope, and variable power resistors with slide-type wirewound, has also been set up. The power resistors connected to the secondary circuit have been utilized as loads during the tests. The experimental set-up is shown in Fig.3. Different scenarios have been explored in order to highlight how the transmitted power depends on the distance and mutual position of the coils, and on the load value.

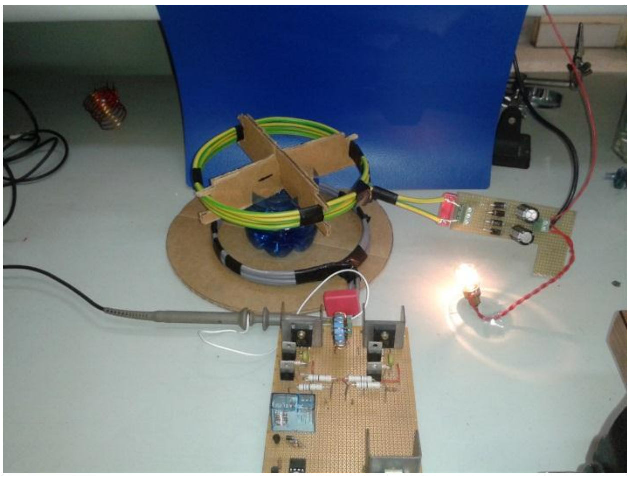

Fig.3 –. Prototype of the power transmission system utilized for the experimental study.

Power versus distance measurements have been obtained taking the ratio between the square value of the rectified voltage measured across the load and the load resistance. Measurements have been performed for different distances between the primary and secondary coil, keeping the coils parallel to each other and with their center aligned. In the experiments the secondary coil was connected to a resistive load, characterized by low resistance (20 Ω). Table 1 shows the transmitted power for different values of the distance between the coils, ranging from 1 up to 24 cm.

TABLE 1, POWER TRANSMITTED TO A SECONDARY CIRCUIT LOADED BY A 20 Ω RESISTOR VERSUS DISTANCE BETWEEN COILS.

Distance [cm]	Power [W]
1	61.25
3	45.00
4	31.25
8	8.45
16	0.45
24	0.05

Moreover, power transmission efficiency has been determined by taking the ratio between the power absorbed by the primary circuit and that delivered to the load; the values obtained in the experiment are given in Table 2.

TABLE 2, POWER TRANSMISSION FFICIENCY VERSUS DISTANCE BETWEEN COILS.

Distance [cm]	Efficiency
1	0.8507
3	0.7500
4	0.6510
8	0.3912
16	0.0250
24	0.0052

Successively, the experiments have been repeated in the presence of a higher resistance load (200 Ω). The transmitted power for the same distances considered above is given in Table 3. Due to a minor loading effect on the resonant tank at the secondary side, the typical behavior of a resonant circuit can be observed. The transmitted power shows a maximum equal to 6.48 W at a distance equal to 8 cm, in correspondence of which the efficiency of the power transmission system is 32%.

TABLE 3, POWER TRANSMITTED TO A 200 Ω RESISTOR VERSUS DISTANCE BETWEEN COILS.

Distance [cm]	Power [W]
1	5.6785
3	5.7800
4	5.7460
8	6.4800
16	1.4450
32	0.0288

Actually, it is the load resistance that is responsible of the power demand of the remote equipment. While in the presence of high power demands the transmitted power definitely decreases upon the distance, a finite short distance between the coils can be tolerated or even planned for light power demands.

The distance between the coils, together with the capacitance, inductance and resistance parameters, also affects the operating frequency of the system. In fact, altering the geometry of the system determines changes of the auto and mutual inductances of the coupled circuits. The oscillatory architecture anyway automatically settles to an operating frequency that grants the maximum power transmission for that configuration. Table 4 gives the operating frequency versus distance between coils. In this experiments it can be observed that the relative inductance increment seen at the primary circuit, which is caused by less flux cancellation, consequent to the lengthened distance between it and the secondary coil, makes the operating frequency decrease from 168 kHz down to 122.9 kHz.

TABLE 4, OPERATING FREQUENCY AS A FUNCTION OF THE DISTANCE BETWEEN COILS. MEASUREMENTS HAVE BEEN PERFORMED WHEN THE SECONDARY CIRCUIT IS LOADED BY A 200 Ω RESISTOR.

Distance [cm]	Frequency [kHz]
1	168.00
3	165.00
4	143.00
8	130.00
16	122.80
32	122.90

Keeping the two coils perfectly parallel at a distance between the respective planes equal to 12 cm with their own orthogonal axes parallel to each other but misaligned, the effects of coils misalignments have also been investigated (Fig.4). Starting from perfect axial alignment conditions, the secondary coil has been gradually moved away in order to have its axis parallel but at a distance from the axis of the primary coil. The distance between the axes orthogonal to the planes hosting the coils states the alignment mismatch. Table 5 gives the power transmitted to the secondary coil loaded by a 200 Ω resistor for misalignments ranging from 0 to 16 cm.

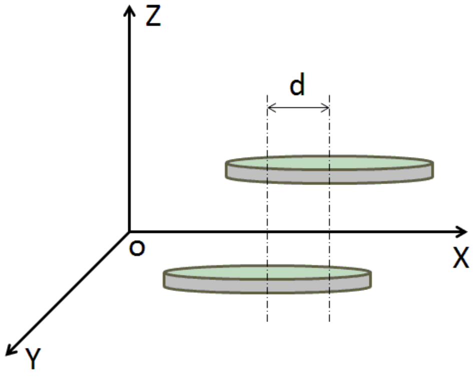

Fig.4, Parallel coils with their own orthogonal axes parallel to each other but misaligned by *d* cm.

Finally, orthogonal coils positions, have been considered to verify if WPT can take advantage by deploying more primary coils in vertical walls surrounding a platform hosting the secondary coil. Table 6 shows the transmitted power versus distance for a system made up of one vertical coil and one horizontal coil. The edge of the vertical coil is tangent to the horizontal platform hosting the secondary coil, i.e. the center of the vertical coil is at 7 cm height upon the horizontal platform; the orthogonal axes of the two coils are kept coplanar. At a distance equal to -7 cm the vertical coil is positioned in the plane that also contains the axis of the horizontal coil.

TABLE 5, EFFECTS OF MISALIGNMENT ON THE POWER TRANSMISSION SYSTEM.

Distance [cm]	Power [W]
0	6.4800
1	6.4800
2	6.1250
4	3.9200
8	1.6200
10	0.7200
12	0.2450
16	0.0098

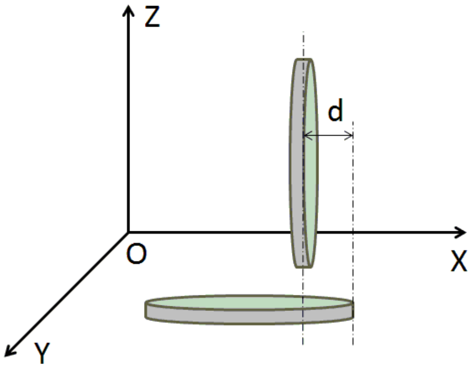

Fig.5, Schematic of the geometry characterized by orthogonal coils.

TABLE 6, EFFECTS OF ORTHOGONALLY POSITIONING OF THE PRIMARY AND SECONDARY COIL.

Distance [cm]	Power [W]
-7	1.0513
-6	1.4965
-5	1.8050
-4	2.1632
-3	2.4865
-2	3.0258
0	3.6450
2	3.1250
3	2.3544
4	1.4112
5	0.8192
6	0.2813
7	0.0085

VII. CONCLUSION

The role of the wireless power transmission technology based on resonant coupled coils has been discussed with reference to two classes of applications. It has been shown that both contactless recharging and batteryless supply can take advantage from this technology.

Contactless recharging involves the possibility of keeping grid disconnected an electrical equipment, or more precisely its internal battery, without giving up to its recharging, letting for example robotic vehicles to autonomously and reliably afford recharge when low battery state is signaled.

Batteryless supply can support the functioning of remote wireless equipment, often deployed in networked architectures, that have become more and more widespread due to their fast installation and easy re-positioning. Batteryless supply represents a much robust solution with respect to ambient energy harvesting or scavenging proposals to avoid back-up batteries. Nonetheless, the perspective of less used batteries needing proper treatment for recycling or disposal, confers additional interest to this approach.

A power transfer system that relies on a resonance-based coupling mechanism and is capable of supporting contactless recharging and batteryless supply has also been discussed. The typical architecture of a system exploiting a relaxation oscillator in the primary circuit has been set up to conduct an experimental study. The results of several tests show the efficiency of the power transfer mechanism both for nominal operative conditions as well as for different ones characterized by deliberate mismatches.

REFERENCES

[1] Akira Oida, Hiroshi Nakashima, Juro Miyasaka, Katsuaki Ohdoi, Hiroshi Matsumoto, Naoki Shinohara "Development of a new type of electric off-road vehicle powered by microwaves trasmitted through air". ScienceDirect, Journal of Terramechanics. 44 (2007) 329-338.

[2] A. Karalis, J. D. Joannopoulos, and M. Soljačić, Efficient wireless non-radiative mid-range energy transfer, Annals of Physics, Jan. 2008, Vol.323, No.1, pp. 34–48.

[3] Gregg E. Maryniak, "Status of International Experimentation in Wireless Power Transmission" SUNSAT Energy Council, 6 Newell Place, Hopewell, NJ 08525, USA. Solar Energy Vol.56, No.1, pp 87-91, 1996.

[4] A. Kurs, A. Karalis, R. Moffatt, J. D. Joannopoulos, P. Fisher, and M. Soljačić, Wireless power transfer via strongly coupled magnetic resonances, Science, 2007, Vol. 317, No.5834, pp. 83–86.

[5] A. P. Sample, D. A. Meyer, and J. R. Smith, "Analysis, Experimental Results, and Range Adaptation of Magnetically Coupled Resonators for Wireless Power Transfer," IEEE Transactions on Industrial Electronics, 2011, Vol.58, No.2, pp.544-554.

[6] N. Kemal Ure, Girish Chowdhary, Tuna Toksoz, Jonathan P. How, Matthew A. Vavrina, and John Vian "An Automated Battery Management System to Enable Persistent Missions With Multiple Aerial Vehicles" IEEE Transactions on Mechatronics, 2015, Vol.20, No.1, pp.275-286.

[7] Bhaskar Saha1, Edwin Koshimoto, Cuong C. Quach, Edward F. Hogge, Thomas H. Strom, Boyd L. Hill, Sixto L. Vazquez, Kai Goebel, "Battery Health Management System for Electric UAVs" IEEEAC paper#1484, Version 2, Updated January 12, 2011.

[8] A. Costanzo, M. Dionigi, F. Mastri, M. Mongiardo, "Rigorous modeling of mid-range wireless power transfer systems based on Royer oscillators," IEEE Wireless Power Transfer (WPT) 2013, May 15-16, Perugia, Italy, pp.69-72.

[9] Aristeidis Karalis, J.D. Joannopoulos, Marin Soljacˇic, "Efficient wireless non-radiative mid-range energy transfer, Science direct Annals of Physic 323 27 April 2007.

[10] William C. Brown, "The History of Wireless Power Transmission" Microwave power transmission systems, 6 Perry Lane, Weston, MA 02193, USA. Solar Energy Vol. 56 No.1, pp. 3-21, 1996.

[11] Yoichi Kurose, Eiji Hiraki, Akito Fukui, and Mutsuo Nakaoka, "Phase Shifted ZVS-PWM High Frequency Load Resonant Inverter for Induction Heated Foam Metal Type Dual Packs Fluid Heater", 29th IEEE Industrial Electronic Society Conference, IECON 2003, Vol.2, pp.1613-1616.

[12] T. Uchiyama, T. Shibata, and K. Mohri "Royer Oscillator Type Pulse Triggered Switching Devices Using YBCO and BSCCO HTcSC Cores" IEEE Translation Journal on Magnetics in Japan, 1992, Vol. 7, No.7, pp.545-550.

[13] Alireza Namadmalan, Javad Shokrollahi Moghani, and Jafar Milimonfared, "A Current-Fed Parallel Resonant Push-Pull Inverter with a New Cascaded Coil Flux Control for Induction Heating Applications" Journal of Power Electronics, Vol. 11, No. 5, September 2011.

[14] B. L. Cannon, J. F. Hoburg, D. D. Stancil, and S. C. Goldstein, "Magnetic Resonant Coupling As a Potential Means for Wireless Power Transfer to Multiple Small Receivers," IEEE Trans. Power Electron., 2009, Vol.24, No.7, pp. 1819–1825.

[15] J.A. Sabatè, V Vlatkovic, R. B. Ridley, and F. C. Lee "High-voltage, High Power, ZVS, Full-bridge PWM Converter Employing an Active Snubber", APEC '91. Conference Proceedings, 1991, pp.158-163.

[16] C. U. Yaisom, W. KJmmgern and S. Nitta, "The Study and Analysis of The Conducted EMI Suppression on Power MOSFET Using Passive Snubber Circuits" 3rd International Symposium on Electromagnetic Compatibility, 2002, pp.561-564.

[17] L. Angrisani, G. d'Alessandro, M. D'Apuzzo, M. D'Arco, "Enabling induction and wireless power transmission technologies aimed at supplying remote equipment in critical logistic scenarios", IEEE Workshop on Measurement & Networking, 7-8 Oct 2013, Naples, ITALY, pp. 184-188.

[18] L. Angrisani, G. d'Alessandro, M. D'Arco, D. Accardo, G. Fasano, "A Contactless Induction System for Battery Recharging of Autonomous Vehicles", IEEE Workshop on Metrology for Aerospace, 29-30 May 2014, Benevento, ITALY.

[19] L. Angrisani, F. Bonavolontà, G. d'Alessandro, M. D'Arco "Inductive power transmission for wireless sensor networks", IEEE Workshop on Environmental, Energy and Structural Monitoring Systems, 17-18 September 2014, Napoli, ITALY.

Journal of Energy Challenges and Mechanics
http://www.nscj.co.uk/JECM/

ISSN 2056-9386
Volume 1 (2014) issue 4, article 3

Calculation of CO_2 freezing points in mixtures using SRK and PR EoSs

使用 SRK 和 PR 状态方程计算混合物中二氧化碳的凝固点

Giorgia De Guido*, Stefano Langè, Stefania Moioli and Laura Annamaria Pellegrini

[1]*Dipartimento di Chimica, Materiali e Ingegneria Chimica "G. Natta", Politecnico di Milano, Piazza Leonardo da Vinci 32, I-20133 Milano, ITALY*

giorgia.deguido@polimi.it

Accepted for publication on 29th November 2014

Abstract - **Global greenhouse gas (GHG) emissions have grown in comparison to pre-industrial levels. Under this scenario, several solutions have been suggested to reduce GHG emissions. Carbon dioxide capture and storage (CCS) is one of the key mitigation actions that have been proposed to meet this goal. Capture of CO_2 can be effectively applied to large point sources, like natural gas production facilities, in order to separate CO_2 from other gaseous products as a concentrated stream which can be readily transported to a storage site. Cryogenic CO_2 removal methods have been widely studied recently as a technology which offers some advantages in comparison with conventional solutions in case of those natural gas reserves that were previously considered uneconomic due to the presence of significant amounts of acidic gas components (carbon dioxide and hydrogen sulfide). Furthermore, cryogenic CO_2 removal methods can capture CO_2 in a liquid form, making its geological storage relatively easy. Some cryogenic removal technologies are based on the formation of solid CO_2 while in other processes particular attention is required to avoid the formation of dry ice. As a result, in both cases, it is necessary to be able to predict the conditions at which CO_2 can freeze-out. A thermodynamic method has been proposed for modeling the solubility of carbon dioxide in pure light hydrocarbons and hydrogen sulfide and in multicomponent mixtures. It is based on the use of a cubic equation of state (EoS) for the calculation of fugacity coefficients in the liquid and vapor phases. The Soave-Redlich-Kwong and the Peng-Robinson EoSs have been chosen in this work since they are widely used in natural gas processing systems. As for the fugacity of CO_2 as a pure component in the solid phase, it is expressed in terms of proper regressed parameters (enthalpy of fusion, specific heat difference between liquid and solid and melting temperature) of the freezing component. The focus is a detailed analysis of the method performances by means of a comparison with experimental data, when available. The addition of hydrogen sulfide and nitrogen to the CO_2-containing mixture is studied to understand how they affect carbon dioxide freezing points.**

Keywords – **Carbon dioxide, Freeze-out, Solubility, SRK, PR**

I. INTRODUCTION

Climate change is definitely one of the most serious challenges to be faced. Since pre-industrial times atmospheric greenhouse gas (GHG) concentrations have markedly increased as a result of increasing emissions of GHGs due to human activities. In particular, total anthropogenic GHG emissions reached the highest levels in human history from 2000 to 2010 at an average rate of 2.2% per year compared to 1.3% per year between 1970 and 2000. Among all major direct GHGs related to human activities, CO_2 from fossil fuel combustion and in industrial processes plays a significant role, with 76% of total GHG emissions in 2010 [1]. In this scenario, mitigation strategies are intended to stabilize GHG concentrations in the atmosphere at a level to prevent harmful consequences on either human or ecological well-being. With respect to the energy supply sector, these strategies include options to mitigate GHG emissions from the extraction, transport and conversion of fossil fuels through CO_2 capture and storage (CCS). This would allow fossil fuels to continue to be used in the future, without significantly contributing to climate change. Many technologies currently exist for separation and capture of CO_2 from gas streams in power plants [2]. They are often classified into oxyfuel, pre- and post- combustion processes. Post-combustion processes are considered the most realistic technology [3] in the short term because they can be retrofitted to already operating power plants and industries. Several post- combustion processes have been developed, including physical and/or chemical absorption, adsorption, membranes and cryogenics, depending on the characteristics of the flue gas stream. The use of cryogenic processes is worth considering when the concentration of CO_2 in the flue gas is high [4]. They are also of great interest in the natural gas purification industry for the removal of CO_2 to produce what is known as pipeline quality natural gas. In particular, cryogenic technologies allow to exploit also those gas reserves that were considered uneconomic in the past due to the high content of acidic components. Nowadays they have been taken into consideration to face the extensive switching from coal to gas as a way for a reduction of GHG emissions. For all these reasons, great attention has been recently devoted to low-temperature processes which possess many potential advantages, including the production of liquid CO_2 which can be readily transported by pipeline. Some cryogenic processes can be classified as solid-based CO_2 capture processes. Some examples are CO_2 capture by anti-sublimation [5], the Controlled Freeze Zone^{TM} technology (CFZ^{TM}) [6] and the cryogenic CO_2 capture (CCC) process [7]. On the contrary, other cryogenic processes avoid the formation of dry ice. The Ryan-Holmes process, for example, avoids solids formation in a cryogenic distillative separation of acid gases by adding a solids-preventing agent such as one or more C_2-C_5 alkanes [8]. A novel distillation process [9] eliminates solid CO_2 build-up by performing distillation in two columns operated at high and low pressures, respectively. In all these processes the prediction of CO_2 freezing points is key for process design. In the literature it has been reported that unreliable CO_2 freezing predictions are being made by several of the commercial process simulators typically used by gas processors [10]. Therefore, the aim of the work is to provide a reliable thermodynamic tool for accurately predicting CO_2 freezing points.

II. THERMODYNAMIC FRAMEWORK

Some empirical correlations based on CO_2 freeze-out experiments have been developed to predict the liquid freezup curves [11]. However, they are not trustable enough to be used for industrial applications. The typical approach for performing every kind of equilibria calculations is based on equating partial fugacities for each component in each phase. In the case of solid-liquid-vapor equilibria calculations (SLVE), Eq. (1)-(3) hold at equilibrium:

$$f_i^S(T,P) = \hat{f}_i^L(T,P,\underline{x}) \quad (1)$$

$$f_i^S(T,P) = \hat{f}_i^V(T,P,\underline{y}) \quad (2)$$

$$\hat{f}_i^L(T,P,\underline{x}) = \hat{f}_i^V(T,P,\underline{y}) \quad (3)$$

where $f_i^S(T,P)$, $\hat{f}_i^L(T,P,\underline{x})$ and $\hat{f}_i^V(T,P,\underline{y})$ stand for the fugacity of component i in the solid, liquid and vapor phase, respectively.

Two approaches are typically used to solve equilibria calculations: the activity coefficient or the equation of state (EoS) approach. They basically differ for the way in which the partial fugacity in the liquid phase is expressed, which affects the form of Eq. (1) either for SLE or SLVE calculations.

The activity coefficient approach has been used in several papers which deal with SLE calculations and consequently involve Eq. (1) only, which is written as:

$$f_i^S(T,P) = \gamma_i x_i f_i^L(T,P) \quad (4)$$

Therefore, the activity coefficient approach requires the estimation of the activity coefficient, γ_i, for the solubility, x_i, to be found. Myers and Prausnitz [12] have calculated the activity coefficient from Scatchard's equation [13] to describe the equilibrium between pure solid CO_2 and a saturated solution of CO_2 in a liquid solvent. The same equation has been used by Preston and Prausnitz [14], Dixon and Johnston [15] and Shen and Lin [16] for obtaining liquid-phase activity coefficients. On the contrary, Gmehling et al. [17] have estimated the activity coefficient from the group-contribution method UNIFAC, while Eggeman and Chafin [18] have chosen the Non-Random Two-Liquid (NRTL) equation.

Eggeman and Chafin [18] have also studied the equation of state approach either for SLE or for SVE calculations. When the equation of state approach is used, Eq. (1) is rewritten as:

$$f_i^S(T,P) = P x_i \hat{\phi}_i^L(T,P,\underline{x}) \quad (5)$$

They have chosen a standard form of the Peng-Robinson (PR) equation of state to calculate fugacity coefficients, with binary interaction parameters k_{ij}s derived from VLE regressions. The same equation of state has been selected by ZareNezhad and Eggeman [11] for predicting CO_2 freezing points of hydrocarbon liquid (SLE) and vapor (SVE) mixtures. However, in this case k_{ij}s have been assumed to be temperature-dependent and this dependency has been found by minimization of the difference between experimental and calculated freezing temperatures. Shen and Lin [16] have used both the PR and the Soave-Redlich-Kwong (SRK) equations of state to calculate the solubility of carbon dioxide in saturated liquid methane. The equation of state approach has been also preferred by Feroiu et al. [19], Xu et al. [20], Yazdizadeh et al. [21, 22] and Kikic et al. [23] to calculate the solubility of solid compounds in supercritical fluids. For modeling solid-fluid equilibria at high pressures also Seiler et al. [24] have decided to describe the non-ideality of the liquid phase by means of an equation of state, that is the SAFT equation of state. Tang and Gross [25] have used the same equation reported by Seiler et al. [24], but they have used the PCP-SAFT equation of state instead.

In this work, cubic equations of state with proper adaptive parameters have been applied to predict CO_2 freezing points in systems containing hydrocarbons, hydrogen sulfide and nitrogen.

III. PROPOSED METHOD

In this work, the equation of state approach has been chosen in order to describe the solid-liquid-vapor equilibrium which may establish in some cryogenic processes aimed at removing CO_2 from gaseous streams. Equilibria calculations are based on the equality (Eq. (6)) between the fugacity of CO_2 (i.e., the freezing component) in the solid phase and its fugacity in the liquid phase, at the system temperature and bubble pressure. The partial fugacity in the liquid phase is expressed in terms of the fugacity coefficient as in the right-hand side of Eq. (6), which is obtained by means of an EoS. The SRK [26] and PR [27] EoSs have been used for comparison.

$$f_{CO_2}{}^{S}(T,P) = P \cdot x_{CO_2} \cdot \hat{\phi}_{CO_2}{}^{L}(T,P,\underline{x}) \tag{6}$$

The pressure in Eq. (6) is the bubble pressure calculated according to Eq. (3), since a three-phase (SLV) equilibrium is considered.

The fugacity of CO_2 in the solid phase can be written taking into account the rigorous thermodynamic relation which allows to express it as a function of the fugacity in the liquid phase, at the same temperature and pressure. By integrating the definition of the fugacity of a pure component introduced by Lewis between the liquid and solid phase at the system temperature and pressure (that is the bubble pressure in case of SLVE calculations) and by substituting the chemical potential of the pure component with the molar Gibbs free energy, the molar Gibbs energy change $\Delta g_{L\rightarrow S}(T,P)$ for pure CO_2 in going from the liquid to the solid phase can be related to the fugacities in the corresponding phases:

$$\Delta g_{L\rightarrow S}(T,P) = RT \ln\left(\frac{f_{CO_2}{}^{S}(T,P)}{f_{CO_2}{}^{L}(T,P)}\right) \tag{7}$$

The left-hand side of Eq. (7) can be related to the corresponding enthalpy and entropy changes by:

$$\Delta g_{L\rightarrow S}(T,P) = \Delta h_{L\rightarrow S}(T,P) - T\Delta s_{L\rightarrow S}(T,P) \tag{8}$$

The thermodynamic cycle in Fig. 1 provides a method to evaluate the enthalpy and entropy changes in Eq. (8).

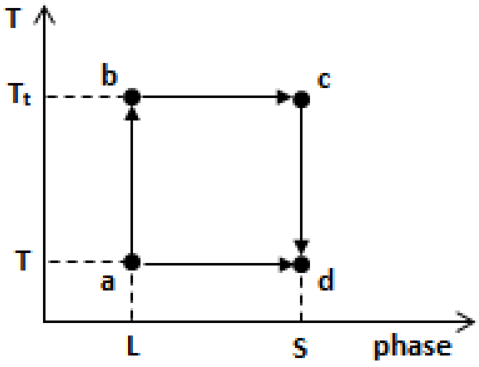

Fig.1, Thermodynamic cycle for the derivation of an expression for the ratio $f_i^S(T,P)/ f_i^L(T,P)$.

Since both the enthalpy and entropy are state functions, the change between two states depends only on the initial and final state of the system but does not depend on the way in which the system acquires those states. Therefore, the enthalpy change can be calculated according to Eq. (9) by following the path *a→b→c→d*, where T_t represents the triple point temperature.

$$\begin{aligned}\Delta h_{L\rightarrow S}(T,P) &= \Delta h_{a\rightarrow b} + \Delta h_{b\rightarrow c} + \Delta h_{c\rightarrow d} \\ &= \int_{T}^{T_t} c_P^L(T)dT - \Delta h_m(T_t) + \int_{T_t}^{T} c_P^S(T)dT \\ &= \int_{T}^{T_t} \left[c_P^L(T) - c_P^S(T)\right]dT - \Delta h_m(T_t)\end{aligned} \tag{9}$$

Similarly, the entropy change can be calculated according to Eq. (10).

$$\begin{aligned}\Delta s_{L\rightarrow S}(T,P) &= \Delta s_{a\rightarrow b} + \Delta s_{b\rightarrow c} + \Delta s_{c\rightarrow d} \\ &= \int_{T}^{T_t} \frac{c_P^L(T)}{T}dT - \frac{\Delta h_m(T_t)}{T_t} + \int_{T_t}^{T} \frac{c_P^S(T)}{T}dT \\ &= \int_{T}^{T_t} \frac{c_P^L(T) - c_P^S(T)}{T}dT - \frac{\Delta h_m(T_t)}{T_t}\end{aligned} \tag{10}$$

As reported by [28], some simplifications can be made. Firstly, the difference between the liquid and solid heat capacities can be assumed to be constant. Secondly, the triple point temperature can be substituted by the normal melting temperature, since for most substances there is little difference between the two, as for the enthalpies of fusion at these two temperatures. Therefore, under these assumptions, the ratio of the fugacity of CO_2 in the solid and liquid phase in Eq. (7) can be expressed as follows:

$$\begin{aligned}\ln\frac{f_{CO_2}{}^{S}(T,P)}{f_{CO_2}{}^{L}(T,P)} &= \frac{\Delta h_m}{RT_m}\left(1-\frac{T_m}{T}\right) + \\ &\frac{\Delta c_P(T_m - T)}{RT} - \frac{\Delta c_P}{R}\ln\frac{T_m}{T}\end{aligned} \tag{11}$$

Eq. (11), also reported by Soave [29], can be combined with Eq. (6), leading to the final result for the freezing point of CO_2 in a mixture at the triple point, which depends only on the properties of the solute (Eq. (12)).

$$x_{CO_2} = \frac{\phi_{CO_2}{}^{L}(T,P)\exp\left[\frac{\Delta h_m}{RT_m}\left(1-\frac{T_m}{T}\right) + \frac{\Delta c_P}{R}\left(\frac{T_m}{T} - 1 - \ln\frac{T_m}{T}\right)\right]}{\hat{\phi}_{CO_2}{}^{L}(T,P,\underline{x})} \tag{12}$$

IV. ADAPTIVE PARAMETERS

As shown in Eq. (11), the fugacity of CO_2 in the solid phase strongly depends on its heat of fusion, Δh_m, on the difference between its liquid and solid heat capacities and on its melting temperature, T_m. These physical quantities have been assumed as adaptive parameters and have been determined by regression of experimental data of sublimation temperature and solid vapor pressure [30-33]. The regressed parameters have been obtained by minimization of the following objective function:

$$f_{ob} = \sum_{j=1}^{Npt} err_j^2 \tag{13}$$

where *Npt* is the total number of points and err_j is calculated as:

$$err_j = \ln f^{S}_{CO_2}(T_j, P_j) - \ln f^{L}_{CO_2}(T_j, P_j) - \left[\frac{\Delta h_m}{RT_m}\left(1 - \frac{T_m}{T_j}\right) + \frac{\Delta c_P (T_m - T_j)}{RT_j} - \frac{\Delta c_P}{R} \ln \frac{T_m}{T_j} \right] \qquad (14)$$

The regressed values, which depend on the EoS chosen for calculations, are reported in Table 1, along with experimental data [34-36] for a comparison aimed at verifying the physical congruity of the proposed method.

TABLE 1, PARAMETERS INVOLVING PROPERTIES OF THE SOLID PHASE

Parameters	SRK EoS	PR EoS	Exp.
$\Delta h_m/R/T_m$	4.5769	4.6774	4.6266 [36]
$\Delta c_P/R$	1.4792	0.9179	1.7145 [34]
T_m (K)	216.39	216.16	216.59 [35]

The values of $\Delta h_m/R/T_m$ and T_m are in good agreement with experimental data, whereas a higher discrepancy has been found for $\Delta c_P/R$, especially for the PR EoS. However, in our opinion, the obtained values can be considered physically consistent and they have been used in the following for SLVE calculations.

Also binary interaction parameters have been assumed as adaptive parameters in order to improve the description of the thermodynamic behavior of systems involving the solid phase. New values of k_{ij}s (Table 2) for both SRK and PR EoSs have been obtained by regression of experimental solubility data of binary mixtures containing CO_2 and *n*-alkanes at low temperatures [37]. Also the value of the binary interaction parameters for the CO_2-H_2S pair has been optimized by regression of experimental data [35] of vapor and liquid composition along V-L-$CO_{2,solid}$ locus for this pair of compounds. The regressed parameters have been obtained by minimization of the same objective function as in Eq. (13), but this time err_j is calculated as:

$$err_j = \left| x_{j,calc} - x_{j,\exp} \right| \qquad (15)$$

TABLE 2, OPTIMIZED VALUES OF BINARY INTERACTION PARAMETERS OBTAINED WITH THE PROPOSED METHOD FOR SRK EOS AND PR EOS

Mixture	SRK EoS	PR EoS
CO_2-C1	0.1243	0.1230
CO_2-C2	0.1332	0.1281
CO_2-C3	0.1235	0.1185
CO_2-C4	0.1150	0.1109
CO_2-C5	0.1067	0.1007
CO_2-C6	0.1021	0.0991
CO_2-H_2S	0.1020	0.0992

In this work k_{ij}s for hydrocarbon-hydrocarbon pairs have been taken from ASPEN HYSYS® [38], as well as those for the H_2S-hydrocarbon pairs and for the N_2-CH_4 pair. They are reported in Table 3. It is worth noticing that k_{ij}s for hydrocarbon-hydrocarbon pairs have the same values for the SRK and PR EoSs.

TABLE 3, VALUES OF BINARY INTERACTION PARAMETERS TAKEN FROM ASPEN HYSYS® [38] FOR PAIRS OTHER THAN THOSE INVOLVING CARBON DIOXIDE

Mixture	SRK EoS	PR EoS
C1-C2	0.0022	0.0022
C1-C3	0.0068	0.0068
C1-C4	0.0123	0.0123
C1-C5	0.0179	0.0179
C1-C6	0.0235	0.0235
C1-H_2S	0.0888	0.0850
C1-N_2	0.0312	0.0360
C2-C3	0.0013	0.0013
C2-C4	0.0041	0.0041
C2-C5	0.0076	0.0076
C2-C6	0.0114	0.0114
C2-H_2S	0.0862	0.0840
C3-C4	0.0008	0.0008
C3-C5	0.0027	0.0027
C3-C6	0.0051	0.0051
C3-H_2S	0.0925	0.0750
C4-C5	0.0005	0.0005
C4-C6	0.0019	0.0019
C4-H_2S	0.0626	0.0600
C5-C6	0.0004	0.0004
C5-H_2S	0.0709	0.0650
C6-H_2S	0.0570	0.0600

V. FREEZING POINTS OF CO2 IN BINARY MIXTURES

The composition of the liquid phase along solid-liquid-vapor locus of binary mixtures containing CO_2 obtained by means of the proposed method has been compared with experimental data available in the literature. Such data have been collected by Kurata [37] from other literature sources [39-42]. The calculated liquid molar fraction of carbon dioxide is in good agreement with experimental data, as shown by the values of Average Absolute Deviation (AAD) reported in Table 4 and calculated according to the following equation:

$$AAD = \frac{\sum_{j=1}^{Npt} \left| x_{j,calc} - x_{j,\exp} \right|}{Npt} \qquad (16)$$

TABLE 4, AVERAGE ABSOLUTE DEVIATIONS OBTAINED WITH THE PROPOSED METHOD, BOTH WITH SRK EOS AND PR EOS, FOR BINARY MIXTURES

Mixture	AAD SRK EoS	AAD PR EoS
CO_2-C1	0.0374	0.0391
CO_2-C2	0.0122	0.0118
CO_2-C3	0.0274	0.0259
CO_2-C4	0.0340	0.0316
CO_2-C5	0.0543	0.0537
CO_2-C6	0.0706	0.0698
CO_2-H_2S	0.0152	0.0158

Results are shown in Fig. 2 for the system comprising CO_2 and methane. No appreciable difference is found between the SRK and PR EoSs for all the investigated binary systems.

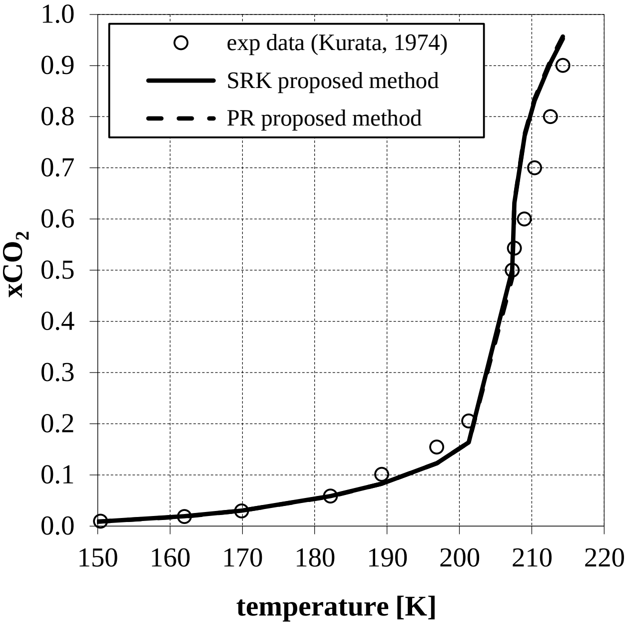

Fig.2, CO_2 freezing points for the CO_2-methane mixture, obtained experimentally [37] and with the proposed method (SRK and PR EoSs).

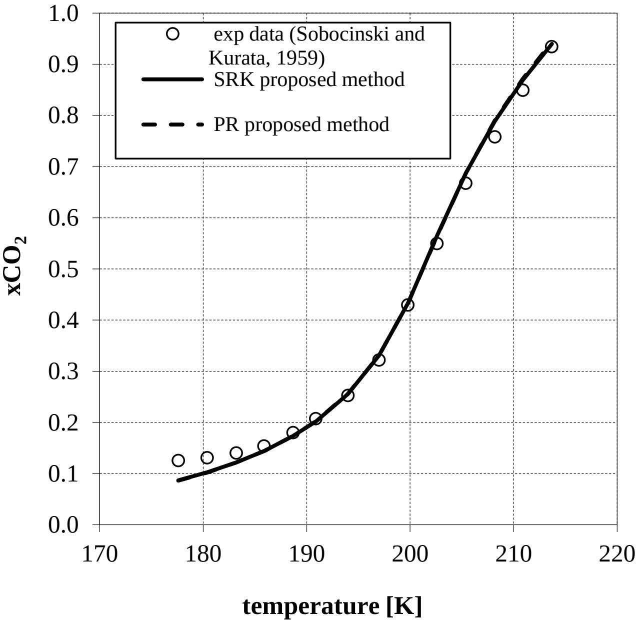

Fig.3, CO_2 freezing points for the CO_2-H_2S system, obtained experimentally [35] and with the proposed method (SRK and PR EoSs).

The comparison with the experimental data reported by Sobocinski and Kurata [35] is shown in Fig. 3 and suggests that the proposed method allows a reliable prediction of dry ice formation also in systems containing H_2S. This is particularly important in cryogenic gas purification processes which aim at reducing the content of acidic components, including H_2S. In comparison with results reported in [43] for the same system with a different binary interaction parameter, the present results also prove the importance of using optimized $k_{ij}s$ to achieve phase equilibrium estimations that are in good agreement with experimental evidence. The performances of the proposed method have been also evaluated by comparing the predicted vapor molar fraction of carbon dioxide with the experimental one. A good agreement with experimental data has been obtained as proved by the obtained AAD values for the two EoSs, which are 0.0126 and 0.0049 for SRK and PR EoSs, respectively.

VI. FREEZING POINTS OF CO2 IN MULTICOMPONENT MIXTURES

Experimental data of mixtures composed of more than one *n*-alkane and CO_2 have been used to validate the proposed method. Data have been taken from [44]. According to the phase rule, a ternary system has two degrees of freedom to completely fix the solid-liquid-vapor equilibrium state. In addition to the temperature, the liquid molar fraction of the second component in mixture has been chosen as the second variable. In the quaternary system containing carbon dioxide, methane, ethane and propane, the number of degrees of freedom is three. The variables to be specified in addition to the temperature have been the ratio of the liquid molar fraction of methane and ethane and the ratio of the liquid molar fraction of methane and propane. The obtained AAD values are reported in Table 5 and the predicted values of the CO_2 molar fraction in the liquid phase along solid-liquid-vapor locus are reported in Fig. 4 for a comparison with the experimental data for the CO_2-methane-ethane system. It can be outsourced that the proposed method allows a reliable representation of the SLVE also for multicomponent mixtures, only requiring parameters relevant to CO_2 alone and binary interaction parameters k_{ij}s.

TABLE 5, AVERAGE ABSOLUTE DEVIATIONS OBTAINED WITH THE PROPOSED METHOD, BOTH WITH SRK EOS AND PR EOS, FOR MULTICOMPONENT MIXTURES

Mixture	AAD SRK EoS	AAD PR EoS
CO_2-C1-C2	0.0158	0.0167
CO_2-C1-C3	0.0168	0.0157
CO_2-C1-C4	0.0251	0.0249
CO_2-C2-C3	0.0345	0.0341
CO_2-C1-C2-C3	0.0155	0.0164

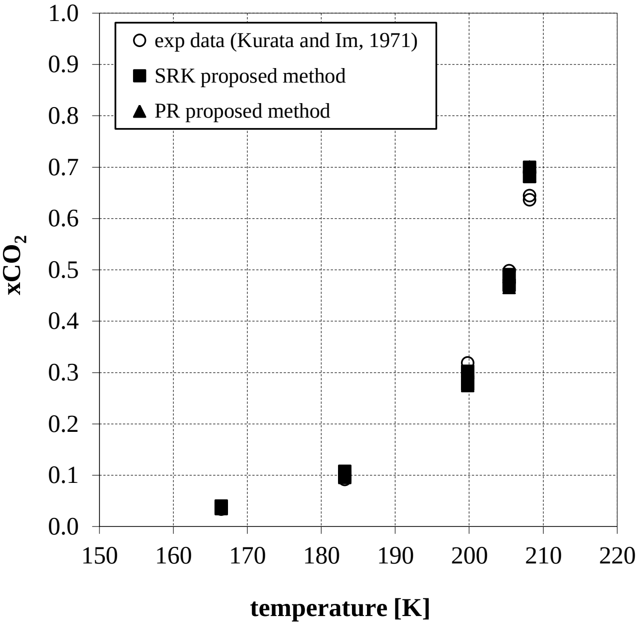

Fig.4, CO_2 freezing points for the CO_2-C1-C2 system, obtained experimentally [44] and with the proposed method (SRK and PR EoSs).

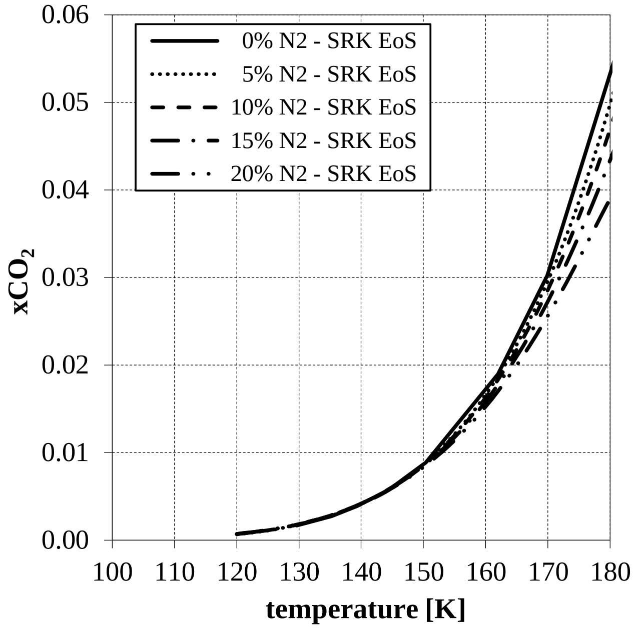

Fig.5, CO_2 freezing points for the CO_2-N_2-C1 system, obtained with the proposed method (SRK EoS).

In [43] the effect of the presence of hydrogen sulfide in mixtures containing carbon dioxide and methane is studied and it is shown that the addition of such a component with a higher boiling point than methane increases the solubility of carbon dioxide in the liquid phase.

Likewise, it is interesting to analyze the effect of the presence of nitrogen in a carbon dioxide-methane mixture. Indeed, Lokhandwala et al. [45] have reported that studies performed by the Gas Research Institute reveal that about 14% of known natural gas reserves in the United States are subquality due to a high nitrogen content. Cryogenic processes are among the main technologies used for natural gas denitrogenation. In order to completely define the solid-liquid-vapor equilibrium state of the ternary system comprising CO_2, nitrogen and methane, the liquid molar fraction of nitrogen has been fixed in addition to the temperature. The nitrogen liquid molar fraction has been varied in the range 5%-20%. The binary interaction parameters for the CO_2-N_2 pair have been taken from [46]. Fig. 5 shows that the presence of nitrogen does not affect the CO_2 freezing point below a temperature of about 150 K, irrespective of the nitrogen content. On the contrary, at higher temperatures as the amount of nitrogen in mixture increases the CO_2 freeze-out problem is likely to occur at lower CO_2 liquid molar fraction. Although Fig. 5 shows the results obtained by means of SRK EoS, they are similar to those obtained when the PR EoS is used for SLVE calculations. The observed effect due to the presence of nitrogen is in agreement with the results reported by Shen and Lin [16], although they have performed SLE rather than SLVE calculations.

VII. CONCLUSION

Carbon dioxide freezing points in mixtures containing one or more hydrocarbons and/or non-hydrocarbon compounds should be properly predicted, especially when dealing with cryogenic CO_2 capture to control climate change. In this paper, a thermodynamic method for calculating CO_2 freezing points is presented. It is based on the use of cubic equations of state and of proper adaptive parameters obtained by regression of experimental data of CO_2 sublimation temperature and solid vapor pressure and of CO_2 solubility in binary mixtures. The proposed method has been validated by comparison with experimental data of equilibrium compositions along the solid-liquid-vapor loci of both binary and multicomponent systems. The agreement of the obtained results with experimental data shows the reliability of the proposed method in the representation of solid-liquid-vapor equilibrium calculations. The proposed method has been also used to predict the effect of the addition of nitrogen to CO_2-methane mixtures. It has been concluded that CO_2 freezing points are slightly affected by the presence of nitrogen in the low-temperature region. On the contrary, as the temperature increases the CO_2 freeze-out problem is more likely to occur for higher nitrogen contents.

NOMENCLATURE

c_P = heat capacity at constant pressure
f = fugacity
g = molar Gibbs free energy
h = enthalpy
k_{ij} = binary interaction parameter between component *i* and *j*
P = pressure

R = gas constant
s = entropy
T = temperature
T_m = melting temperature
T_t = triple point temperature
x = molar fraction in liquid phase
y = molar fraction in vapor phase

Greek symbols
γ = activity coefficient
Δ = difference
φ = fugacity coefficient

Superscripts
L = liquid
S = solid
V = vapor

Subscripts
i = component
m = melting

Abbreviations
AAD = average absolute deviation
EoS = equation of state
Exp = experimental
Npt = number of points
PR = Peng-Robinson
SRK = Soave-Redlich-Kwong

REFERENCES

[1] O. Edenhofer, R. Pichs-Madruga, Y. Sokona, E. Farahani, S. Kadner, K. Seyboth, A. Adler, I. Baum, S. Brunner, P. Eickemeier, B. Kriemann, J. Savolainen, S. Schlömer, C. von Stechow, T. Zwickel and J.C. Minx, "Climate Change 2014: Mitigation of Climate Change. Contribution of Working Group III to the Fifth Assessment Report of the Intergovernmental Panel on Climate Change," 2014.

[2] A. B. Rao and E. S. Rubin, "A Technical, Economic, and Environmental Assessment of Amine-Based CO_2 Capture Technology for Power Plant Greenhouse Gas Control," *Environmental Science & Technology,* vol. 36, pp. 4467-4475, 2002.

[3] M. J. Tuinier, *et al.*, "Cryogenic capture using dynamically operated packed beds," *Chemical Engineering Science,* vol. 65, pp. 114-119, 2010.

[4] P. Riemer, "Greenhouse gas mitigation technologies, an overview of the CO_2 capture, storage and future activities of the IEA Greenhouse Gas R&D programme," *Energy Conversion and Management,* vol. 37, pp. 665-670, 1996.

[5] D. Clodic and M. Younes, "CO_2 capture by anti-sublimation Thermo-economic process evaluation," in *Fourth Annual Conference on Carbon Capture & Sequestration*, Alexandria, USA, 2005.

[6] B. T. Kelley, *et al.*, "Controlled Freeze Zone™ for developing sour gas reserves," *Energy Procedia,* vol. 4, pp. 824-829, 2011.

[7] S. Burt, *et al.*, "Cryogenic CO_2 Capture to Control Climate Change Emissions," in *The 34th International Technical Conference on Clean Coal & Fuel Systems May*, 2009.

[8] A. S. Holmes and J. M. Ryan, "Cryogenic distillative separation of acid gases from methane," US 4318723 United States Mon Dec 14 09:26:01 EST 2009 EDB-84-183118 English, 1982.

[9] L. A. Pellegrini, "Process for the removal of CO_2 from acid gas," ed: Google Patents, 2014.

[10] T. Eggeman and S. Chafin, "Pitfalls of CO_2 freezing prediction," in *82nd Annual Convention of the GPA. San Antonio, USA: GPA*, 2003.

[11] B. ZareNezhad and T. Eggeman, "Application of Peng–Rabinson equation of state for CO_2 freezing prediction of hydrocarbon mixtures at cryogenic conditions of gas plants," *Cryogenics,* vol. 46, pp. 840-845, 2006.

[12] A. Myers and J. Prausnitz, "Thermodynamics of solid carbon dioxide solubility in liquid solvents at low temperatures," *Industrial & Engineering Chemistry Fundamentals,* vol. 4, pp. 209-212, 1965.

[13] J. Hildebrand and R. Scott, "The Solubility of Nonelectrolytes, Reinhold Publ," *Corp, New York,* 1950.

[14] G. Preston and J. Prausnitz, "Thermodynamics of solid solubility in cryogenic solvents," *Industrial & Engineering Chemistry Process Design and Development,* vol. 9, pp. 264-271, 1970.

[15] D. J. Dixon and K. P. Johnston, "Molecular thermodynamics of solubilities in gas antisolvent crystallization," *AIChE Journal,* vol. 37, pp. 1441-1449, 1991.

[16] T. Shen and W. Lin, "Calculation of Carbon Dioxide Solubility in Liquefied Natural Gas," *Int. J. Chem. Eng. Appl,* vol. 2, pp. 366-371, 2011.

[17] J. G. Gmehling, *et al.*, "Solid-liquid equilibria using UNIFAC," *Industrial & Engineering Chemistry Fundamentals,* vol. 17, pp. 269-273, 1978.

[18] T. Eggeman and S. Chafin, "Beware the pitfalls of CO_2 freezing prediction," *Chemical Engineering Progress,* vol. 101, pp. 39-44, 2005.

[19] V. Feroiu, *et al.*, "Modelling the Solubility of Solid Aromatic Compounds in Supercritical Fluids," *REVISTA DE CHIMIE,* vol. 61, pp. 685-690, 2010.

[20] G. Xu, *et al.*, "Reliable computation of high-pressure solid-fluid equilibrium," *Industrial & Engineering Chemistry Research,* vol. 39, pp. 1624-1636, 2000.

[21] M. Yazdizadeh, *et al.*, "Thermodynamic modeling of solubilities of various solid compounds in supercritical carbon dioxide: Effects of equations of state and mixing rules," *The Journal of Supercritical Fluids,* vol. 55, pp. 861-875, 2011.

[22] M. Yazdizadeh, *et al.*, "Applications of cubic equations of state for determination of the solubilities of industrial solid compounds in supercritical carbon dioxide: A comparative study," *Chemical Engineering Science,* vol. 71, pp. 283-299, 2012.

[23] I. Kikic, *et al.*, "A thermodynamic analysis of three-phase equilibria in binary and ternary systems for applications in rapid expansion of a supercritical solution (RESS), particles from gas-saturated solutions (PGSS), and supercritical antisolvent (SAS)," *Industrial & Engineering Chemistry Research,* vol. 36, pp. 5507-5515, 1997.

[24] M. Seiler, *et al.*, "Modeling of solid/fluid phase equilibria in multicomponent systems at high pressure," *Chemical Engineering & Technology,* vol. 24, pp. 607-612, 2001.

[25] X. Tang and J. Gross, "Modeling the phase equilibria of hydrogen sulfide and carbon dioxide in mixture with hydrocarbons and water using the PCP-SAFT equation of state," *Fluid Phase Equilibria,* vol. 293, pp. 11-21, 2010.

[26] G. Soave, "Equilibrium constants from a modified Redlich-Kwong equation of state," *Chemical Engineering Science,* vol. 27, pp. 1197-1203, 1972.

[27] D.-Y. Peng and D. B. Robinson, "A new two-constant equation of state," *Industrial & Engineering Chemistry Fundamentals,* vol. 15, pp. 59-64, 1976.

[28] J. M. Prausnitz, *et al.*, *Molecular thermodynamics of fluid-phase equilibria*: Pearson Education, 1998.

[29] G. S. Soave, "Application of the redlich-kwong-soave equation of state to solid-liquid equilibria calculations," *Chemical Engineering Science,* vol. 34, pp. 225-229, 1979.

[30] W. Giauque and C. Egan, "Carbon dioxide. The heat capacity and vapor pressure of the solid. The heat of sublimation. Thermodynamic and spectroscopic values of the entropy," *The Journal of Chemical Physics,* vol. 5, pp. 45-54, 2004.

[31] G. W. C. Kaye and T. H. Laby, *Tables of physical and chemical constants: and some mathematical functions*: Longmans, Green and co., 1921.

[32] D. R. Stull, "Vapor pressure of pure substances. Organic and inorganic compounds," *Industrial & Engineering Chemistry,* vol. 39, pp. 517-540, 1947.

[33] T. Tables, "Selected values of properties of chemical compounds," *Thermodynamic Research Center Data Project, Texas A&M University, College Station,* vol. 971, pp. 2605-2609, 1974.

[34] AspenTech, *ASPEN Properties Databank*®. Burlington, MA: AspenTech, 2010.

[35] D. Sobocinski and F. Kurata, "Heterogeneous phase equilibria of the hydrogen sulfide–carbon dioxide system," *AIChE Journal,* vol. 5, pp. 545-551, 1959.

[36] M. Zabransky, *et al.*, "Heat capacity, melting enthalpies, and melting temperatures of pure liquid inorganic compounds," *Chem. Prum,* vol. 38, pp. 67-73, 1988.

[37] F. Kurata, *Solubility of solid carbon dioxide in pure light hydrocarbons and mixtures of light hydrocarbons*: Gas Processors Association, 1974.

[38] AspenTech, *Aspen HYSYS*®. Burlington, MA: AspenTech, 2010.

[39] J. Brewer and F. Kurata, "Freezing points of binary mixtures of methane," *AIChE Journal,* vol. 4, pp. 317-318, 1958.

[40] J. Davis, *et al.*, "Solid-liquid-vapor phase behavior of the methane-carbon dioxide system," *AIChE Journal,* vol. 8, pp. 537-539, 1962.

[41] R. H. Jensen and F. Kurata, "Heterogeneous phase behavior of solid carbon dioxide in light hydrocarbons at cryogenic temperatures," *AIChE Journal,* vol. 17, pp. 357-364, 1971.

[42] U. K. Im, *Solubility of Solid Carbon Dioxide in Certain Paraffinic Hydrocarbons: Binary, Ternary and Quaternary Systems*: University of Kansas, 1970.

[43] G. De Guido, *et al.*, "Thermodynamic method for the prediction of solid CO_2 formation from multicomponent mixtures," *Process Safety and Environmental Protection,* vol. 92, pp. 70-79, 2014.

[44] F. Kurata and K. U. Im, "Phase equilibrium of carbon dioxide and light paraffins in presence of solid carbon dioxide," *Journal of Chemical & Engineering Data,* vol. 16, pp. 295-299, 1971.

[45] K. A. Lokhandwala, *et al.*, "Nitrogen removal from natural gas using membranes," in *Proceedings of the Natural Gas Conference, Federal Energy Technology Center (FETC), Houston, Texas, March,* 1999.

[46] L. A. Pellegrini, *et al.*, "Prediction of vapor–liquid equilibrium for reservoir mixtures with cubic equations of state: Binary interaction parameters for acidic gases," *Fluid Phase Equilibria,* vol. 326, pp. 45-49, 2012.

Journal of Energy Challenges
and Mechanics

http://www.nscj.co.uk/JECM/

ISSN 2056-9386
Volume 1 (2014) issue 4, article 4

Impact of temperature on CO_2 storage in a saline aquifer based on fluid flow simulations and seismic data (Ketzin pilot site, Germany)

基于流体模拟和地震数据（德国 Ketzin 试点）研究温度对咸水层二氧化碳封存的影响

Alexandra Ivanova[1*], Christopher Juhlin [2], Ursula Lengler[1], Peter Bergmann[1]

Stefan Lüth[1], Thomas Kempka[1]

[1]*Helmholtz Centre Potsdam, GFZ German Research Centre for Geosciences, Potsdam D-14473, Germany*
[2]*Department of Earth Sciences, Uppsala University, Uppsala SE-75236, Sweden*

aivanova@gfz-potsdam.de

Accepted for publication on 28th November 2014

Abstract - **Temperature is one of the main parameters influencing CO_2 properties during storage in saline aquifers, since it controls along with pressure the phase behavior of the CO_2/brine mixture. When CO_2 replaces brine as a free gas it is known to affect the elastic properties of porous media considerably. In order to track the migration of geologically stored CO_2 in a saline aquifer at the Ketzin pilot site (Germany), 3D time-lapse seismic data were acquired by means of a baseline (pre-injection) survey in 2005 and monitor surveys in 2009 and 2012. At Ketzin, CO_2 was injected from 2008 to 2013 in a sandstone reservoir at a depth of about 630 - 650 m. In total about 67 kilotons of CO_2 were injected. The present study is devoted to the 4D seismic dataset of 2005 - 2009. The temperature in the storage reservoir near the injection well was observed to have increased from 34 °C in 2005 to 38 °C in 2009. This temperature increase led us to investigate the impact of temperature on the seismic response to CO_2 injection and on our estimations of spatial CO_2 mass distribution in the reservoir based on the Ketzin 4D seismic data. Both temperature scenarios in the reservoir of 2005 and 2009 were studied using multiphase fluid flow modeling. The isothermal simulations carried out for both 34°C and 38°C show that the impact of temperature on the seismic response is minor, but the impact of temperature on the CO_2 mass estimations is significant. The multiphase fluid flow simulations show a strong temperature impact on CO_2 density stressing the need for temperature monitoring in a CO_2 storage reservoir to support quantitative observations in the storage complex.**

Keywords – **CO_2 storage, Seismic modeling, Multiphase flow, Reservoir temperature.**

I. INTRODUCTION

It is well known that temperature along with pressure are the major parameters influencing CO_2 storage (e.g. [1], [2]). However, only few experimental data are reported in the temperature and pressure range of interest [2, 3]. At the Ketzin pilot site in Germany [4], CO_2 was injected from 2008 to 2013 at about 640 m depth with the temperature data being continuously acquired with a permanently installed system [5]. Ketzin is the first European onshore pilot scale project for CO_2 storage in a saline aquifer [4]. This storage site is situated on an anticlinal structure hosting sandstones of the heterogeneous Triassic Stuttgart Formation [4] which serve as a reservoir. These sandstones vary in thickness between 15 and 30 m [4] at the injection site. The CO_2 storage reservoir is sealed by an approximately 200 m thick cap rock section of playa-type mudstones of the Weser and Arnstadt Formations [4]. Totally about 67 kilotons of CO_2 were injected at Ketzin. A number of reservoir simulations have been performed to enhance the understanding of CO_2 migration at the Ketzin pilot site [4, 6]. Reservoir simulations and 4D seismic data analysis were successfully integrated at the Sleipner CO_2 storage site [7]. This motivated us to integrate these two methods also at the Ketzin pilot site. 3D time-lapse seismic data were acquired by means of a baseline (pre-injection) survey in 2005 [8] and two monitor surveys in 2009 [9] and 2012 [10]. The present study is devoted to the 4D seismic dataset of 2005 - 2009. The 3D baseline seismic survey [8] at the Ketzin pilot site revealed a sequence of clear reflections from approximately 150 ms to 900 ms two-way traveltime in the stacked volume. In 2009, a subset of this baseline survey was acquired around the injection well after approximately 22–25 kilotons of CO_2 had been injected [9]. This 3D seismic repeat survey showed a pronounced time-lapse amplitude anomaly at the top of the storage reservoir [9] demonstrating that CO_2 can be monitored under such conditions. As a follow up, CO_2 seismic signatures were used to make estimates on imaged amount of injected CO_2. These estimates were done in [9] neglecting the impact of the reservoir temperature. However the temperature increased by 4° by 2009 due to the injection [3]. At the same time there was no significant change in the values of the reservoir temperature 50 m and 112 m away from the injection well [3]. Based on these observations, it appears likely that the CO_2 density was 260 kg/m3 at the injection point (38°C) in 2009, whereas it was near 320 kg/m3 in the more distant part of the plume, close to the ambient temperature (34°C) [3]. In order to investigate the impact of the reservoir temperature variation on the interpretation of the 4D seismic data at Ketzin, we deduce quantitative CO_2 mass estimates for the both reservoir temperature values in 2009 (34°C and 38°C). In the first step we apply seismic forward modeling using so far established petrophysical models for the Ketzin reservoir sandstone [3]. Subsequently, CO_2 mass estimations based on reservoir isothermal simulations for both temperature scenarios are compared to other ones obtained by the in situ CO_2 saturation logging in [9].

II. Multiphase Fluid Flow Simulations

We apply in this study 2D multiphase fluid flow simulations to account for the lateral variability in the petrophysical properties of the storage formation at Ketzin and, in turn, on the 4D seismic data regarding the impact of the reservoir temperature on the fluid migration. Hydrogeological studies at the Ketzin pilot site [11] have shown that a 2D radially symmetric model of the upper part (33 m) of the Stuttgart Formation can be used to interpret the 3D data acquired near the injection well. This model accounts for the presence of channel sandstones in the reservoir that are the most favorable for CO_2 migration and contains effective porosities in the range of 20–25% [4]. Initial reservoir conditions and rock properties within the reservoir sandstone and the surrounding mudstone are listed in Table 1 [3]. They were assumed to be spatially constant for the flow simulations, which were performed using the numerical program TOUGH2 version 2.0 [12] with the fluid property module ECO2N, which was designed for application to the geologic storage of CO_2 in saline aquifers [13]. Two isotherm cases were considered with a constant reservoir porosity of 20%, one where the reservoir temperature is 34°C and the other where the reservoir temperature is 38°C (Table 1).

The resulting simulated CO_2 saturation does not differ significantly between the two scenarios (less than 5%), whereas the CO_2 density is notably lower for the higher temperature case (Fig. 1). In the vicinity of the injection well, the difference in CO_2 density is up to 20% and on average 12%.

TABLE 1, Material properties and initial conditions used for multiphase fluid flow simulations [3]

Material Property		
Porosity [-]	0.20	
Horiz. perm. [m²]	$80 \cdot 10^{-15}$	
Vertic. perm. [m²]	$26.7 \cdot 10^{-15}$	
Residual liquid saturation S_{lr} [-]	0.15	
Residual gas saturation S_{gr} [-]	0.05	
Initial Conditions		
Pressure [MPa]	6.28	
Temperature [°C]	34	38
Salinity [wt.-% NaCl]	20.0	

III. Qualitative Impact of Reservoir Temperature on Seismic Data

In order to investigate the impact of temperature in the reservoir on the 4D seismic data at the Ketzin pilot site, CO_2 saturation and CO_2 density, as well as the thickness of the CO_2 layer obtained by multiphase fluid flow simulations are used as input to seismic modeling [3]. The forward seismic modelling was done for three points: the injection well and two other points, distanced 50 m and 112 m away from the injection well (Fig. 1).

The resulting synthetic seismic differences of both the 34°C and 38°C options look very similar [3]. The synthetic difference (repeat-base) seismograms from near the top of the reservoir agree reasonably well with the real difference seismograms (repeat-base) for the injection well and for the distance of 50 m away from this well [3]. However, obvious disagreements are found 112 m away from the injection well, may be because the velocity model from [3] for this location is too simplified. Seismic amplitude differences between the 38°C and 34°C scenarios correspond to less than 1% of the amplitude values of the baseline. Since the normalized root mean square differences in the 3D time-lapse data are greater than 10% [3] these temperature effects in the reservoir will not be resolvable with surface seismic methods at the Ketzin pilot site.

IV. Quantitative Impact of Reservoir Temperature on Seismic Data

Although it is not possible to determine the reservoir temperature from the seismic amplitude at the Ketzin pilot site in 2005 and 2009, we are able to study here the impact of the reservoir temperature on quantitative interpretation of the seismic data [3]. We apply the method of volumetric estimation of [9] to both the 34°C and 38°C reservoir temperature scenarios and estimate the mass of the injected CO_2 based on the above simulations.

As in [9] we put the minimum and maximum bounds in our quantification at the beginning and end of the 3D seismic repeat acquisition campaign in 2009 at Ketzin. The minimum total mass (25.6 kilotons) and the maximum total mass (29.3 kilotons) for the 34°C scenario are considerably higher than the amount of injected CO_2 at the time of the repeat survey in 2009 (21.1–24.2 kilotons). However, for the 38°C option, the

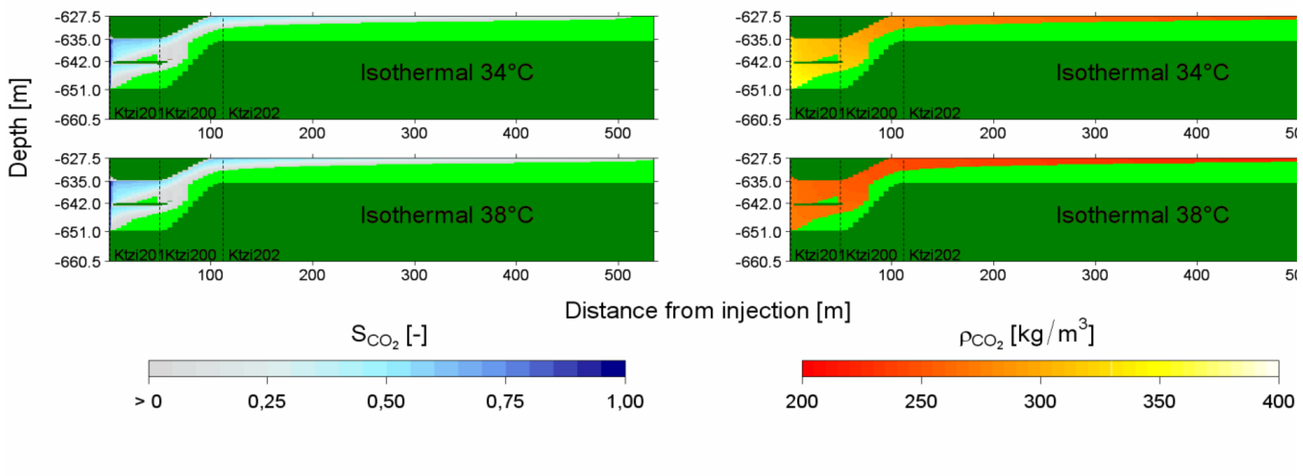

Fig.1, Simulated distributions of CO_2 saturation (left panel, blue scale) and density (right panel, yellow–orange scale) with an isothermal temperature of 34°C and 38°C for October 28, 2009 [3]. CO_2 free rocks of the Stuttgart Formation are dark green. Parts of this formation saturated with brine only are indicated with the light green color. "Ktzi201" is the injection well. "Ktzi200" and "Ktzi202" are observation wells distanced 50 m and 112 m away from the injection well respectively [4].

minimum mass (22.3 kilotons) and maximum mass (22.8 kilotons) are completely within the bounds of the amount of injected CO_2 (21.1–24.2 kilotons) and match well with the CO_2 mass estimation from [9] (20.5–23 kilotons). This quantification shows that the impact of the reservoir temperature is considerable when trying to quantify the amount of CO_2 in the subsurface and that it needs to be accurately estimated. Based on this quantification it appears that a significant portion of the reservoir containing CO_2 was at 38°C at the time of the 3D seismic repeat survey in 2009.

III. DISCUSSION

It is likely that in 2009 the simulated scenarios of 38°C and 34°C are representative in the vicinity of the injection well and in the remaining reservoir, respectively. This is based on a measured temperature of approximately 38°C at the injection well in 2009, while at the observation wells distanced 50 m and 112 m away from the injection well the temperature was at 34°C. Since most of the CO_2 was concentrated around the injection well in 2009, the higher temperature value plays an important role in estimating the mass of CO_2 from the seismic data of the real difference seismograms (repeat-base) [3]. The integration of seismic modeling and multiphase fluid flow simulations allows for synthetic time-lapse difference seismograms (repeat-base) that demonstrate the main features of the real seismic data. Taking into account assumptions made constructing the model we consider the correlation between the synthetic and real seismic sections to be satisfactory. But the following points should be considered when evaluating the modeling results. The constant 20% reservoir porosity [3] used for modeling of the temperature effects is probably an over-simplification since the reservoir is quite heterogeneous [4]. In addition, sound waves may have a frequency dependent propagation velocity so that the higher the frequency the higher the speed. Although velocity dispersion is probably present in the Ketzin reservoir sandstones, we do not consider it to be large enough that it could considerably affect the qualitative and quantitative interpretation of our time-lapse seismic data [9].

Besides, our seismic interpretation of the time-lapse 3D dataset 2005-2009 contains an uncertainty contributed by experiments on core samples at 40°C, because temperature in the reservoir at Ketzin was 34°C before the injection and 34-38°C in 2009, respectively. After [14] and [15] temperatures near the CO_2 critical point have just a minor effect on the seismic velocity in sands saturated with brine and CO_2. Via the Gassmann's equations [16] this translates into 9 m/s as the maximum change in Vp between the options of 34°C and 40°C. Therefore, this effect can be disregarded.

The estimation of the CO_2 mass based on the Ketzin 4D seismic data shows that the impact of temperature is significant for the calculations due to its impact on CO_2 density. Hence, temperature monitoring is an important component for quantitative seismic interpretations at a saline aquifer. Using the temperature measured at the injection well at Ketzin in 2009 for the mass estimation results in a better CO_2 mass quantification. This result is completely within the bounds of the known injected CO_2 mass at the beginning and end of 3D seismic repeat acquisition campaign and in very good agreement with the CO_2 mass estimation based on in situ CO_2 saturation logging. Nevertheless, it has to be taken into consideration that the quantitative analysis contains considerable uncertainties as discussed above and in [9].

Future issues to be considered include expanding the temperature range (34–38°C in this study) to be investigated and the resulting effects on the seismic response and the role of the reservoir heterogeneity. It would be also important to investigate the impact of temperature on CO_2 storage at other sites with favorable P-T conditions in the reservoir. A similar approach applied to the impact of pressure in the reservoir would also be important for CO_2 monitoring using 3D time-lapse seismic methods.

IV. CONCLUSIONS

By integrating seismic modeling and multiphase fluid flow simulations, we have estimated the impact of temperature in the reservoir on 4D seismic data from Ketzin. We studied two options, one where the injection was performed at 34°C and the other at 38°C. Results from the multiphase fluid flow simulations show that the difference between these options is small for the CO_2 migration. Likewise, the temperature does not affect significantly the seismic amplitude response, in spite of the fact that CO_2 density is considerably lower for the higher temperature case. Therefore, the modeled time-lapse seismic differences for the two temperature scenarios show that the effect of reservoir temperature is minor for the qualitative analysis of the 4D seismic data from the Ketzin pilot site.

However, the CO_2 mass quantification based on the 4D seismic data from Ketzin using results from the multiphase fluid flow simulations shows that the impact of temperature in the reservoir at the monitoring time is significant for such quantification. This is mostly due to the impact on CO_2 density, which strongly depends on temperature. The simulated CO_2 saturation levels also influence volumetric estimation. The results show that temperature monitoring is very important for quantitative seismic interpretation at the Ketzin pilot site. Using the higher temperature scenario, corresponding to that measured at the injection well, gives a better result for the CO_2 mass. This estimate is completely within the bounds of the true amount of injected CO_2.

V. ACKNOWLEDGEMENT

The European Commission (6th and 7th Framework Program), two German ministries - the Federal Ministry of Economics and Technology and the Federal Ministry of Education and Research - and industry are gratefully acknowledged for funding the Ketzin pilot project since 2004. The ongoing activities are funded within the project COMPLETE by the Federal Ministry of Education and Research within the GEOTECHNOLOGIEN program (this is publication GEOTECH-2217). Further funding is received from VGS, RWE, Vattenfall, Statoil, OMV and the Norwegian CLIMIT programme.

REFERENCES

[1] A. Kumar, M. Noh, G.A. Pope, K. Sepehrnoori, S. Bryant, and L.W. Lake. “Reservoir Simulation of CO_2 Storage in Deep Saline Aquifers,” *SPE J.*, **10**(3), pp. 336-348, 2005.

[2] S. Bachu, and D.B. Bennion. “Dependence of CO_2-brine interfacial tension on aquifer pressure, temperature and water salinity,” *Energy Procedia*, **1** (1), pp. 3157-3164 GHGT-9, 2009.

[3] A. Ivanova, C. Juhlin, U. Lengler, P. Bergmann, S. Lüth, and T. Kempka. “Impact of temperature on CO_2 storage at the Ketzin site based on fluid flow simulations and seismic data,” *International Journal of Greenhouse Gas Control*, 19, pp. 775-784, 2013.

[4] S. Martens, T. Kempka, A. Liebscher, S. Lüth, F. Möller, A. Myrttinen, B. Norden, C. Schmidt-Hattenberger, M. Zimmer, M. Kühn, and The Ketzin Group. “Europe's longest-operating on-shore CO_2 storage site at Ketzin, Germany: a progress report after three years of injection”, *Environmental Earth Sciences*, **67** (2), pp. 323-334, 2012.

[5] J. Henninges, A. Liebscher, A. Bannach, W. Brandt, S. Hurter, S. Köhler, F. Möller, and CO2SINK Group. “P-T-ρ and two-phase fluid conditions with inverted density profile in observation wells at the CO_2 storage site at Ketzin (Germany)”, *Energy Procedia*, **4**, pp. 6085-6090, 2011.

[6] T. Kempka, and M. Kühn. “Numerical simulations of CO_2 arrival times and reservoir pressure coincide with observations from the Ketzin pilot site, Germany”, *Environmental Earth Sciences*, Special Issue, pp. 1–11, doi:10.1007/s12665-013-2614-6, 2013.

[7] R. Arts, O. Eiken, A. Chadwick, P. Zweigel, L. van der Meer, and B. Zinszner. “Monitoring of CO_2 injected at Sleipner using time lapse seismic data” *Energy*, **29**, pp. 1383-1392, 2004.

[8] C. Juhlin, R. Giese, K. Zinck-Jørgensen, C. Cosma, H. Kazemeini, N. Juhojuntti, S. Lüth, B. Norden, and A. Förster. “3D baseline seismics at Ketzin, Germany: the CO2SINK project”, *Geophysics*, **72**, pp. 121-132, 2007.

[9] A. Ivanova, A. Kashubin, N. Juhojuntti, J. Kummerow, J.Henninges, C. Juhlin, S. Lüth, and M. Ivandic. “Monitoring and volumetric estimation of injected CO_2 using 4D seismic, petrophysical data, core measurements and well logging: a case study at Ketzin, Germany”, *Geophysical Prospecting*, **60**(5), pp. 957-973, 2012.

[10] M. Ivandic, C. Juhlin, S. Lüth, P. Bergmann, A. Kashubin, D. Sopher, A. Ivanova, G. Baumann, and J. Henninges. “Geophysical monitoring at the Ketzin pilot site for CO_2 storage: New insights into the plume evolution”, *International Journal of Greenhouse Gas Control*, submitted, 2014.

[11] B. Norden, A. Förster, D. Vu-Hoang, F. Marcelis, N. Springer, and I. Le Nir. “Lithological and petrophysical core-log interpretation in CO2SINK, the European CO_2 Onshore Research Storage and Verification Project”, *SPE Reservoir Evaluation & Engineering*, **13** (2), pp. 179-192, 2010.

[12] K. Pruess, C. Oldenburg, and G. Moridis. ”TOUGH2 User's guide, Version 2.0”, *Lawrence Berkeley National Laboratory Report LBNL-43134*, Berkeley, USA, 1999.

[13] K. Pruess. “ECO2N: A TOUGH2 Fluid Property Module for Mixtures of Water, NaCl, and CO_2“, *Lawrence Berkeley National Laboratory Report LBNL-57952*, Berkeley, USA, 2005.

[14] G. Mavko. “Parameters That Influence Seismic Velocity”*http://pangea.stanford.edu/courses/gp262/Notes/8.SeismicVelocity.pdf*, 2005.

[15] D. Han, M. Sun, and M. Batzle. “CO_2 velocity measurement and models for temperatures up to 200 °C and pressures up to 100 MPa”, *Geophysics*, **75** (3), pp. E123–E129, 2010.

[16] F. Gassmann. “Ueber die Elastizitaet poroeser Medien“, *Vierteljahrsschrift der Naturforschenden Gesellschaft Zuerich*, **96**, pp. 1–23, 1951.

Journal of Energy Challenges and Mechanics
http://www.nscj.co.uk/JECM/

ISSN 2056-9386
Volume 1 (2014) issue 4, article 1

Simulation of multi–stage hydro–fracture development by the SIE method

通过 SIE 方法模拟多级水力裂缝的发展

G.V. Paderin[1*], O.Ya. Izvekov[1], A.N. Galybin[2]

[1]*Moscow Institute of Physics and Technology, Moscow, Russia*
[2]*The Schmidt Institute of Physics of the Earth, RAS, Moscow, Russia*

g.paderin@gmail.com

Accepted for publication on 23rd December 2014

Abstract – **This study deals with 2D simulations of curvilinear multi–stage hydro-fracture growth in a reservoir. The numerical model employs the method of complex singular integral equations, the SIE method. The crack path is found by applying the criterion of maximum tensile stress at the fracture tip. The study investigates the fracture development for different initial spacings between the fractures, in-situ stresses and the values of fluid pressure that can be different for different cracks.**

Keywords – **Hydraulic fractures, Crack growth, Complex singular integral equation**

I. INTRODUCTION

Collective fracture growth driven by internal fluid can be observed in nature and during technological processes. Examples include magma penetration into the crust, which causes dike and sill formation or multistage hydraulic fracturing. Nowadays the latter becomes a widely used procedure of enhancing well productivity in low-permeability reservoirs (Cippola et al. 2009), which requires proper design to provide economic effectiveness of this treatment. Conventional design does not take into account the stress field redistribution induced by the fracture interaction, which affects the crack trajectories and deviate them from the straight path. This can lead to a complex geometry of the fracture system especially in the case when the fractures are placed close to each other. Any fracture developed under the action of internal pressure caused by fluid penetration is further referred to as hydraulic fracture (HF). In this study multi–stage HF growth is modeled. It means that the fracture system is build up subsequently (the next HF starts to grow when the previous one stops). The numerical model is based on the method of singular integral equations (SIE), which provides effective computation of the fracture characteristics used further on for calculations of the fracture path.

II. PROBLEM FORMULATION AND METHOD OF SOLVING

The physical model is based on the mechanics of brittle fracture. Our aim is to calculate quasi-static fracture trajectories; therefore the process of fracture propagation is modeled by a sequence of the stationary states (steps). At each step of fracture growth the plane elastic problem is solved for which we employ the method of complex SIE in the form developed by Savruk (1981). The system of SIE is solved numerically by the method of mechanical quadratures based on the Gauss-Chebyshev quadrature formula (see Savruk, 1981). It is assumed that either the loads or the crack opening displacement (or its derivative) are known on each fracture. On the fractures where the loads are known the crack opening displacement (or its derivative) is the sought function, which is used for calculating the stress intensity factors (SIFs) for the current configuration of the fracture system. We assume that the fracture continue to propagate if the mode I stress intensity factor K_I is greater than the fracture toughness K_{IC}. For crack path simulations we apply the criterion of maximum tensile stress at the crack tip. The fracture closure is checked at every step to ensure that the crack surfaces do not enter into contact over any part of the crack. The process ends when a certain fracture length is reached or if the crack surfaces start to contact. In the latter case the fracture growth terminates prematurely (certain length is not reached), because the system of SIE does not describe this case and needs to be modified.

III. MULTI-STAGE HF SIMULATION: TWO APPROACHES

To simulate the multi-stage (subsequent) growth we assume that every new fracture appears and starts to grow only after the previous one stops when it achieved certain length, i.e. during the n^{th} stage the n^{th} fracture is the growing one and the length of the (n-1) previously developed cracks are kept equal to an assigned value (same for all fractures). All initial fractures are assumed to be straight and oriented coaxial to the major compressive in-situ stress T_2 (T_1 is the minor compressive in-situ stress). We further assume that these are normalized by the value of pressure in the firstly growing crack (the straight crack shown on the left in all subsequent figures). Therefore, the following constraint is imposed $0<T_1<1$, if $T_1\geq 1$ the hydrofracture cannot grow.

To model multi-stage HF growth we consider two approaches. In the first one we take into account the mutual interaction between the fractures. Physically it means that not only the previously grown crack affects the growing one (direct influence) but also the growing crack affects all previous cracks. In mathematical formulation we impose the in-situ stresses and the fluid pressure in each fracture. While the n^{th} fracture is growing the crack opening displacement (and consequently the SIFs) of the previous n-1 cracks can change their values because of the influence of the growing crack due to increase of its length.

In the second approach we do not take into account the mutual interaction of all cracks. It implies that there is no back influence of the growing HF on the previous ones, so only the previously made cracks affect the growing one. It leads to a different mathematical formulation of the problem. Namely, on the previous (n-1) fracture the crack opening displacements obtained at the previous stages are fixed whereas on the currently growing fracture we impose the load: fluid pressure, in-situ stresses and the stresses caused by the previously grown cracks. As the result it is necessary to solve only one complex SIE instead of n generated in the first approach. Thus, from the computational side the second approach requires less computer resources.

Both approaches are important because they represent two limiting cases. Therefore, the real crack path should lie somewhere between the two trajectories simulated in accordance with these approaches. This is why all of the figures presented in this study show two trajectories obtained by both approaches (the first approach is presented by dashed lines and the second approach by continuous lines).

There are several factors that affect the crack path and in this study we examine some of them.

IV. TRAJECTORY DEPENDENCE ON THE DISTANCE

It is evident that for larger distances between the fractures their interaction is less pronounced. Fig. 1 shows the results of simulation for different relative spacing between the fractures $d/2a$, where d is the distance between the nearest crack centers and $2a$ is the final fracture length. In all cases presented in this paper the units for horizontal and vertical axes are dimensionless length and we specify the final fracture half-length a equal to ten units. Fluid pressure is assumed to be uniform and equal to one unit. The values of the in-situ stresses are equal and do not exceed the fluid pressure. Their value in this case does not affect the fracture trajectories. The mode I stress intensity factor K_I is assumed to be greater than the fracture toughness K_{IC}. It the latter is negligible, then the fracture grows occur for $K_I>0$.

The fracture trajectory is modeled by a polygonal line with equal sides; same for all fractures. Two sides are added symmetrically to the crack ends at every step of fracture growth to the previous configuration. The crack system is formed by adding new fractures from left to right as shown in all figures below.

Simulation shows that the decrease of spacing pushes the cracks to deviate more and more from the straight path as demonstrated in Fig 1a-d. Eventually it leads to fracture closure that initiate termination of further calculations. It should be noted that closure occurs for the crack on the right in Fig. 2.

Fig. 3-5 present the range of simulation of multi-stage HF for in-situ stresses $T_1=0.4$ and $T_2=0.8$ and the fluid pressure of one unit for different dimensionless spacings $d/2a$. At each step of the fracture growth its closure is controlled. The cracks grow until the assigned length. The trajectories obtained by both approaches are closed to each other in most cases.

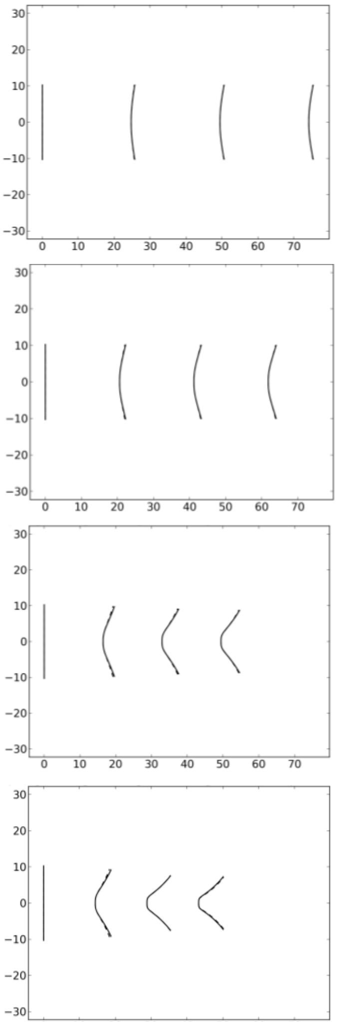

Fig.1, Multi-stage HF driven by fluid pressure of one unit and equal in-situ stresses $T_1=T_2=0.6$ for: a) $d/2a$=1.2 b) $d/2a$=1.0 c) $d/2a$=0.8 d) $d/2a$=0.7.

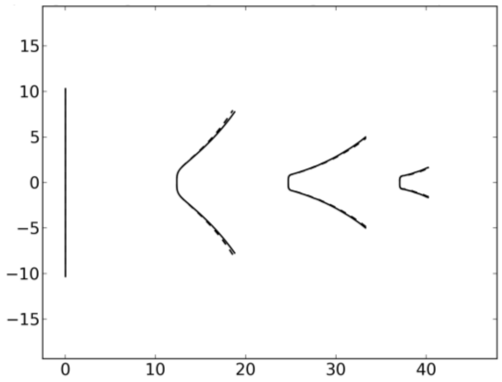

Fig.2, Fracture growth terminates prematurely. Multi-stage HF driven by one unit fluid pressure with equal in-situ stresses of T_1=T_2=0.6 for $d/2a$=0.6.

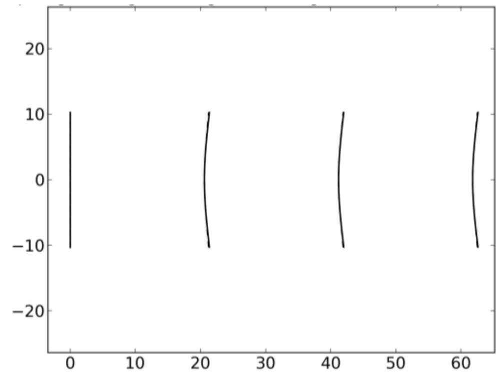

Fig.3, Multi-stage HF driven by one unit fluid pressure; T_1=0.4 and T_2=0.8 for $d/2a$=1.0.

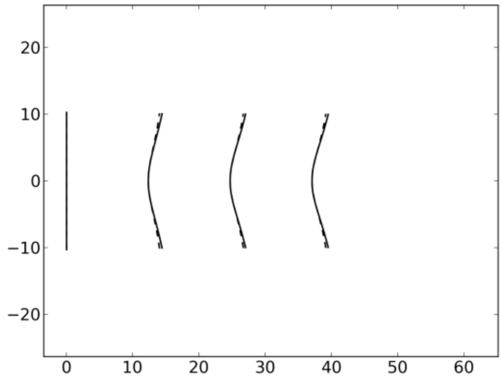

Fig.4, Multi-stage HF driven by one unit fluid pressure; T_1=0.4 and T_2=0.8 for $d/2a$=0.6.

The results of simulation show that the contrast of in-situ stresses makes the crack path to be less curvilinear, which can compensate its further bending due to decrease of relative spacing. Therefore it is possible to reduce the initial spacing between the multi-stage HF in reservoirs subjected to high contrast in-situ stresses (Fig. 5) as compared to the case of hydrostatic in-situ stresses (Fig. 2).

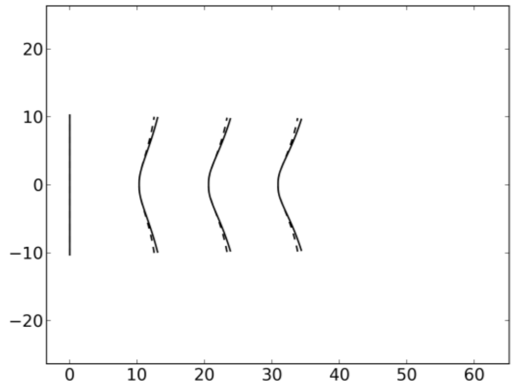

Fig.5, Multi-stage HF driven by one unit fluid pressure; T_1 =0.4 and T_2=0.8 for $d/2a$=0.5.

V. THE INFLUENCE OF THE IN-SITU STRESSES

Let us introduce the in-situ stress ratio $k = T_2/T_1$, $k>1$ that characterizes the contrast of in-situ stresses. We have already conducted some simulation for k =1 (Fig. 1- 2) and k =2 (Fig. 3-5). The results of simulation for k =4 (these are not presented in the paper) is similar to the case k=2. Thus, it can be concluded that further increase of the in-situ stress ratio makes no significant effect on the curvature of the trajectories as presented in Fig. 5. Furthermore, usually in the real reservoir the value of k is between 1 and 2. Fig.6 and 7 show the results of stimulation for k =1.1 and k =1.23.

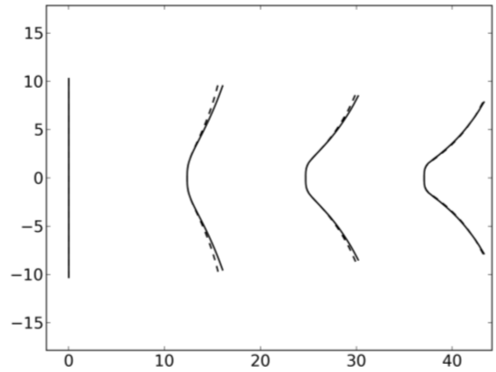

Fig.6, Multi-stage HF driven by fluid pressure of one unit; T_1=0.727 and T_2=0.8 (k=1.1) and $d/2a$=0.6.

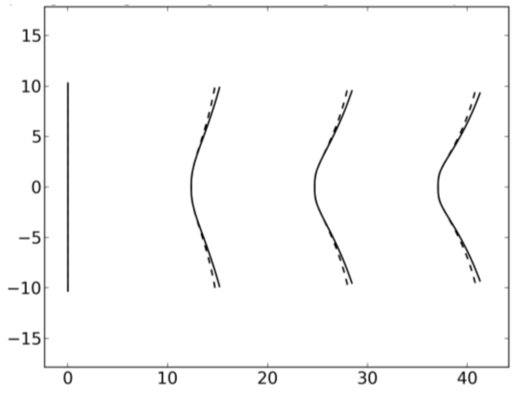

Fig.7, Multi-stage HF driven by fluid pressure of one unit; T_1=0.65 and T_2=0.8 (k=1.23) and $d/2a$=0.6.

The results of simulation (see Fig. 2,4,6,7 made for the same spacing $d/2a=0.6$) show that the increase of the in-situ stress ratio leads to straightening of the HF trajectories. Comparing the trajectories in Fig. 2 and Fig. 6 one can notice that even a small stress contrast makes the fracture path straighter. Therefore, the situation presented in Fig. 2 is unlikely to happen in practice.

VI. THE INFLUENCE OF THE DIFFERENT PRESSURES

In all configurations presented above both approaches (with and without mutual integration) produce quite similar trajectories (dashed and continuous lines are hardly distinguishable). However, they can be essentially different as shown further on.

Fig. 8-13 present the results of simulations with different fluid pressures in different HF. In-situ stresses are $T_1=0.4$ and $T_2=0.8$ ($k=2$) for the cases shown in Fig. 8-10; Fig. 11 addresses the case $T_1=T_2=0$; Fig. 12 the case $T_1=T_2=0.6$ ($k=1$); and Fig. 13 the case $T_1=0.65$, $T_2=0.8$ ($k=1.23$). The relative spacing in all these cases is $d/2a=0.5$. Fluid pressures are assumed to be uniform, their values are given by the formula $p_{hf}=q^{s-1}$, where s is the number of the stage (the number of fractures counted from left to right) and $q>1$ is a parameter that vary from figure to figure.

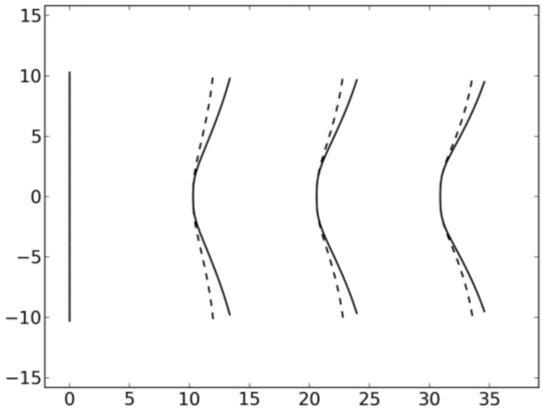

Fig.8, Multi-stage HF driven by fluid pressure phf=qs-1, q=1.1; T1=0.4, T2=0.8 and d/2a=0.5.

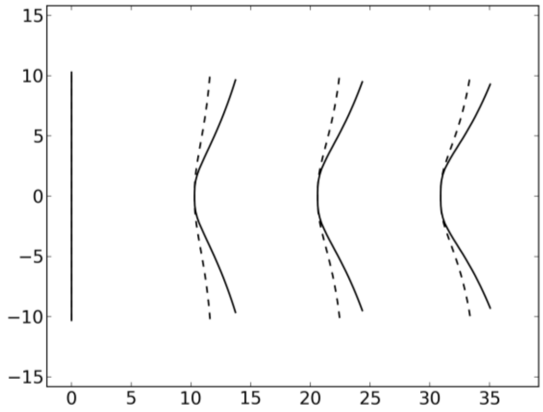

Fig.9, Multi-stage HF driven by fluid pressure $p_{hf}=q^{s-1}$, $q=1.2$; $T_1=0.4$, $T_2=0.8$ and $d/2a=0.5$.

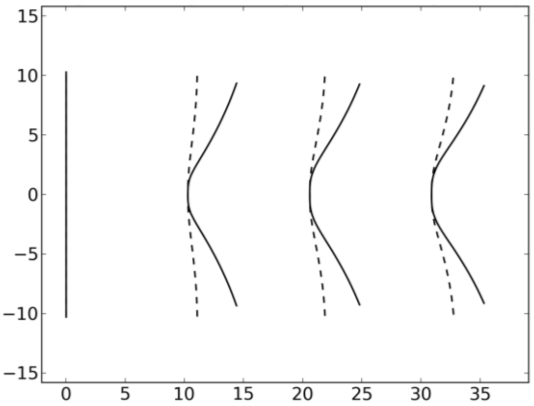

Fig.10, Multi-stage HF driven by fluid pressure $p_{hf}=q^{s-1}$, $q=1.4$; $T_1=0.4$, $T_2=0.8$ and $d/2a=0.5$.

Comparing Fig. 5 and Fig. 8-10 one can notice that the trajectories calculated by the different approaches are essentially different when the pressure rises (by increasing q). They not only deviate from each other, they also show a qualitatively different response on pressure rise. Namely, the crack paths have tendency to straighten if the crack interaction is taken into account. If it is not, they tend to bend more and deviate from the straight line.

Fig. 11-12 depict crack behavior in the case of equal in-situ stresses. They are zero in the configuration presented in Fig. 11 and equal to 0.6 in Fig. 12.

Fig. 13 represents the crack path for in-situ stress ratio $k=1.23$ ($T_1=0.65$, $T_2=0.8$).

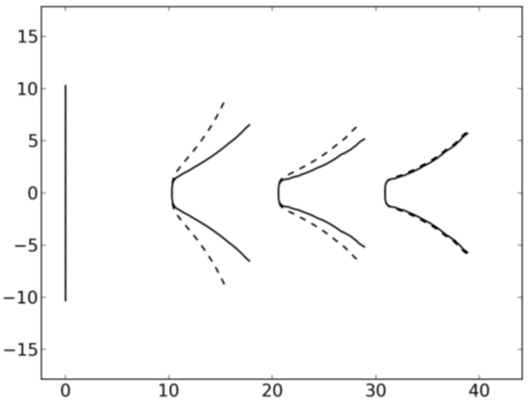

Fig.11, Multi-stage HF driven by fluid pressure $p_{hf}=q^{s-1}$, $q=1.2$; $T_1=T_2=0$ and $d/2a=0.5$.

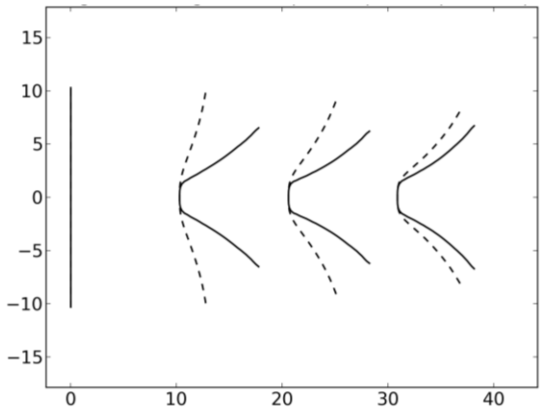

Fig.12, Multi-stage HF driven by fluid pressure $p_{hf}=q^{s-1}$, q=1.2; T_1=T_2=0.6 and $d/2a$=0.5.

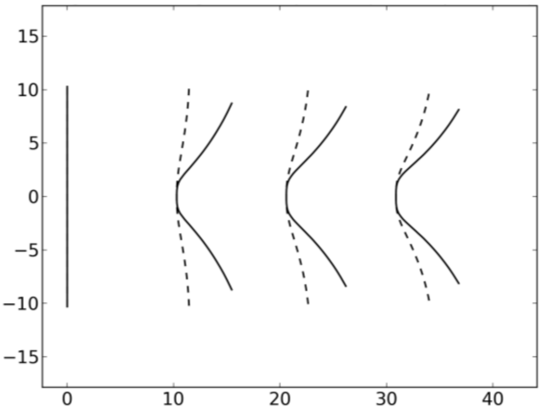

Fig.13, Multi-stage HF driven by fluid pressure $p_{hf}=q^{s-1}$, q=1.2; T_1=0.65 and T_2=0.8 (k=1.23) and $d/2a$=0.5.

The results of simulations presented in Fig.8-13 show that in the case of different fluid pressures the values of the in-situ stresses play a significant role, even if k=1 (especially in simulations without taking into account the mutual interaction of all cracks). It has been found that even small increase of q leads to apparently different trajectories obtained by two approaches.

VII. SHIELDING EFFECT AND ITS COMPENSATION

Let us discuss why the different values of fluid pressure (q>1) strongly affect the crack path. The first reason has already been mentioned, the fractures tend to deviate less from the straight line when the in-situ stress ratio is close to unity (compare the trajectories in Fig.2 and Fig 12). The second reason is, so called, shielding effect. The latter means the decrease of K_I values of the currently growing crack due to influence of the previously grown cracks. Consider the multi-stage HF driven by fluid pressure for in-situ stresses of T_1=0.4 and T_2=0.8 and relevant spacing $d/2a$=0.5. Fluid pressure is equal to one unit in every fracture (equally loaded cracks). The calculated fracture trajectories are presented in Fig.5. The values of the mode I stress intensity factor K_I for the growing crack are summarized in Table I depending on the fracture length, 2a, shown in the first column.

TABLE 1, Mode I SIFs for growing fracture for equally loaded crack

Length	1 stage	2 stage	3 stage	4 stage
0.6	0.58	0.21	0.17	0.16
4.6	1.61	0.65	0.56	0.54
11.0	2.49	1.38	1.24	1.20
19.8	3.35	2.54	2.39	2.34

One can notice significant decrease of K_I for the 2, 3, 4 fractures during their growth compare to K_I for the first stage respectively. In this case the shielding effect can make K_I to be smaller than the fracture toughness (or even negative), which stops fracture growth. Furthermore, if K_I is small then the crack opening is small too. Insufficient crack opening may impede the transfer of proppant along the fracture and eventually decrease the overall productivity of the HF system. Increase of fluid pressure in each following HF is capable to compensate the shielding effect. Table 2 shows the values of K_I for the growing cracks during the simulation for the same configuration except of the values of the fluid pressure specified as $p_{hf}=(1.1)^{s-1}$, where s is the number of the growing HF. The trajectories of this simulation are presented in Fig.8.

Comparing Table 1 and 2 one can notice that the increase of 10% in fluid pressure of the next fracture (q=1.1) provides considerable compensation of the shielding effect.

TABLE 2, Mode I SIFs for the growing fracture for differently loaded cracks

Length	1 stage	2 stage	3 stage	4 stage
0.6	0.58	0.30	0.31	0.34
4.6	1.61	0.92	0.96	1.07
11.0	2.49	1.81	1.96	2.20
19.8	3.35	3.20	3.55	3.97

VIII. CONCLUSION

In this study we have simulated the fracture trajectories during the mutli-stage HF by using the SIE method.

We have analyzed the influence of different factors on the crack trajectories and the stress intensity factors. It was shown the crack paths deviate from the straight line more and more as soon as the spacing decreases. The increase of in-situ stresses ratio (parameter k) forces the crack paths to straighten. Also it was found that the increase of fluid pressure of the next fracture over the previous one is capable of compensating the shielding effect, making the trajectories straighter (especially in the case of hydrostatic in-situ stress field), and reduce the probability of their closure.

ACKNOWLEDGEMENTS

The authors are grateful for the support by Grant for Young Scientists MK-7249.2013.5 and by grants RFBR 13-05-00631 and 14-01-00855.

REFERENCES

[1] C.L. Cipolla, E.P. Lolon, M.J. Mayerhofer and N.R. Warpinski. “Fracture Design Considerations in Horizontal Wells Drilled in Unconventional Gas Reservoirs”. Paper SPE 119366 presented at *the SPE Hydraulic Fracturing Technology Conference*, The Woodlands, Texas, 19-21 January 2009.

[2] M.P. Savruk. *2D problems of elasticity for bodies with cracks.* Kiev: Naukova Dumka, 1981.

Journal of Energy Challenges and Mechanics
http://www.nscj.co.uk/JECM/

ISSN 2056-9386

Volume 1 (2014) issue 4, article 6

The behaviour of biomass char in two direct carbon fuel cell designs

两个直接碳燃料电池设计中生物质炭的行为

Olalekan D. Adeniyi[1*], Bruce C.R. Ewan[2], Mary I. Adeniyi[1], Mukhtar Abdulkadir[1]

[1]*Chemical Engineering Department, Federal University of Technology, PMB 65, Minna, Nigeria*
[2]*Chemical & Biological Engineering Department, University of Sheffield, Mappin Street, Sheffield, S1 3JD, UK*

Lekanadeniyi2002@yahoo.co.uk

Accepted for publication on 11th December 2014

Abstract - **The performances of two fuel cell designs are reported using carbon fuel arising from the pyrolysis of a number of common biomass materials. In the first, a simple design based on carbonate saturated zirconia cloth is used whilst in the second, a proprietary prototyping button cell based on solid oxide technology is investigated. Gold mesh current collectors are used in both cases. Results are presented for the power density and cell voltage versus current density at 800°C and show that peak powers of 70 mW/cm^2 at current densities of 100 mA/cm^2 are achievable and that the more highly engineered solid oxide design will perform better by a factor of around 5 on both measures. The results demonstrate that, with only moderate processing, power generation from biomass using more advanced electrochemical technologies, with higher thermal efficiencies, can make a useful contribution to the overall effort to reduce CO_2 emissions.**

Keywords – **fuel cell, biomass, carbon, current, power, pyrolysis, voltage**

I. INTRODUCTION

The direct carbon fuel cell (DCFC) is a special kind of high temperature fuel cell that directly uses carbon as fuel supplied to the anode and has the potential to reduce the complexities of reforming hydrocarbon raw materials to fuels such as hydrogen. The DCFC has been shown to offer significantly higher thermal efficiencies [1] for electrical power generation compared to combustion routes and even for other fuel cell types using different fuels. The raw materials for powering a DCFC are solid, carbon-rich fuels, and much of the effort in recent years has been devoted to fossil fuel carbon sources, such as coal and petroleum coke. The benefits arising from the use of these fuels in DCFCs are equally available to biomass derived carbon and the overall cycle efficiencies when DCFCs are incorporated into appropriate combined cycles are likely to be higher than those associated with current gasification processes due to the intrinsically higher efficiency of the carbon fuel cell stage of such cycles.

At the higher temperatures normally used for DCFCs (> 600°C), carbon fuel is electro-oxidised to CO_2 at the anode compartment creating electricity [2]. The DCFC is becoming more important because of the various advantages that it offers. Because no heat engines or reformers are needed in the DCFC system it is mechanically simple to build and can be located around biomass sites, thus reducing the cost of transportation, and reducing environmental pollution. The production of tiny carbon particles produced by pyrolysis and used in the DCFC requires less energy and capital than the production of hydrogen-rich fuels used in other fuel cell types. Since carbon oxidation is achieved electrochemically at the anode without direct mixing with air, the CO_2 is created as a pure gas which can be captured and stored as part of a carbon capture and storage (CCS) strategy. This aspect, combined with the potential 50% reduction in CO_2 emissions due to improved thermal efficiency, indicates that low emissions may be achieved at lower energy costs when compared to conventional power plants.

Additional operational benefits include the avoidance of fly ash emissions and the associated capture technologies [1, 3-6]. A DCFC has certain efficiency advantages over other types of fuel cell arising from the nature of the reactants and products and due to the small entropy change (~ 2 J/mol K). The transport of oxygen to a fuel cell anode is conventionally achieved by three routes, using molten carbonates, molten alkali metal hydroxides or using solid electrolytes such as stabilised zirconia. In the present work, the designs use the molten carbonate and solid zirconia electrolyte systems.

Pyrolysis of biomass is used in the production of solid (charcoal), liquid (tar and other organics) and gas products.

Research in the area of pyrolysis is becoming more and more important, because of its many advantages. Many researches have been carried out on biomass pyrolysis, and for the purpose of the DCFC, the char is of particular relevance [7-9]. The relative proportions of pyrolysis products depends on the properties of the source material such as fixed carbon and volatiles content as well as process employed, which includes heating rates and soak temperature. As an example, Onay and Kockar [8] obtained 24 – 31wt% char yield from rapeseed, while Şensöz obtained between 30 – 59wt.% char from pine barks pyrolysis. This paper focuses on the char produced from the pyrolysis of miscanthus straw (M. giganteus), and wood chips from willow (salix) and spruce (picea) and the primary interest is in the behaviour of these chars in a fuel cell device.

II. BIOMASS MATERIALS AND PREPARATION

The biomass samples were chopped into smaller pieces before grinding, which was carried out using a Cross Beater Mill with a sieve size of 2.0 mm. The chopped biomass was added to the mill in stages for effective grinding and the process was repeated three times to obtain the effective particle size before carrying out proximate, ultimate, and calorific value analyses.

The ash and volatile content were measured using a furnace operating at temperature of 750°C and 950°C respectively. The moisture content was determined using an oven operated at 105°C for an hour and the fixed carbon was calculated by difference. The total carbon and hydrogen contents were measured by sample oxidation in a furnace operated at 1350°C and calorific values for the dry samples were determined using a bomb calorimeter.

The biomass samples of particle size of 0.5 to 1.0 mm, were dried at 100°C before pyrolysing in a cylindrical, electrically heated furnace (70 mm diameter). In each pyrolysis cycle, the sample was heated at a rate of 7 °C/min up to the operating temperature of 800°C, and held for 30 min. [9]. Nitrogen gas was used to purge the system at a rate of 4 litre/min, during and after the pyrolysis process until it cooled down to 200°C. The proportion of char produced in each case was in the range 22 - 24wt%, which compares with other reported results for the conditions used. Table 1 summarise the biomass pyrolysed char properties.

TABLE I, PROPERTIES OF BIOMASS CHAR.

Material	Fixed carbon wt.%	Hydrogen wt.%	Calorific Value MJ/kg
Miscanthus	87.37	1.03	29.11
Willow	84.55	1.37	29.56
Spruce	92.96	1.14	32.53

Evidence of graphitic structure in the chars was examined by application of XRD (Cu, Kα) to the powders. These showed broad peaks with maxima in range $2\theta = 22 - 28^o$, which indicates some disordered graphite layers but also a high degree of amorphous carbon and are similar to patterns reported by others for coal samples.

III. PREPARATION OF CARBON FUEL PARTICLES

Each biomass char was ground by ball milling following the same procedure for each material. Size analysis on the samples was carried using laser diffraction sizing and showed that 50% of the weight fell within the particle size range 2.2 -8.1 μm. At the operating temperature of the fuel cell, the fuel is presented as a slurry dispersed in a molten carbonate mixture.

The fuel particles were dispersed in a Li_2CO_3/K_2CO_3 mixture at a concentration of 15 wt.% and the carbonate components were mixed in the ratio of 46.6 wt.% Li_2CO_3 and 53.4 wt.% K_2CO_3, giving a melting point close to 500°C. The carbonates were prepared by initially dissolving in water followed by drying at 100°C and, following fine grinding, were mixed with the biomass carbon to form the fuel mixture for the cell.

IV. FUEL CELLS CONSTRUCTION AND OPERATION

The two fuel cell types employed are identified as molten carbonate (MCFC) and solid oxide (SOFC). For the MCFC the electrolyte consists of the same molten carbonate mixture as was used for the char fuel dispersion, whilst the SOFC consisted of a button cell of yttria stabilised zirconia [11]. For both systems the same overall cell containment was used.

The electrode assembly for each type was held between two open alumina tubes of 24 mm internal diameter, 3 mm wall, and oriented vertically. The end of each tube was held within a closed metal chamber, which included built-in flanges and allowed steel, spring loaded tie bars to be fixed between each end of the system to hold the electrode assemblies in place. The overall length of the tubular assembly was 280 mm.

The lower 80% of the tubular system could then be located within a furnace and the cell operating temperature was monitored locally using a sheathed K-type thermocouple which entered through the upper metal chamber. Inlet and outlet tubes were provided through the upper and lower metal chambers to allow some purging on the anode side and the oxidant gas on the cathode side.

For the MCFC, the electrolyte system consisted of 0.5 mm thick zirconia cloth (ZYW 30A supplied by Zircar Zirconia Inc.) of 25 mm diameter, which was saturated with the molten carbonate mixture at around 600°C. Current collectors in the form of gold mesh, (99.9%, 0.06 mm wire diameter, 65% open area, supplied by Goodfellow) were placed in contact with this electrolyte on both sides, and on the lower cathode side, a ceramic support was provided in the form of a perforated disc of 1.5 mm diameter to maintain good contact between the mesh and the electrolyte disc, and which at the same time allowed air contact. Annular mica rings formed the boundary between the electrode assembly and the upper and lower alumina tubes.

For the SOFC, the central element was a button cell of 25 mm diameter (supplied by Fuel Cell Materials) consisting of an yttria stabilised zirconia electrolyte (150 µm in thickness) and central 12.5 mm diameter anode layer (50 µm thickness) consisting of nickel/zirconia cermet and corresponding cathode layer (50 µm thickness) composed of lanthanum strontium manganite (LSM). The anode side of the button cell as supplied, is in the oxidised form and this was subjected to a reducing atmosphere consisting of 5% hydrogen in nitrogen for 1 hour at 900ºC prior to use. Any subsequent processing steps which required elevated temperatures ensured that the same protective reducing atmosphere was provided. This cell element was further processed with the addition of gold mesh current collectors on anode and cathode sides, which were attached using silver ink to the edges and a further heat cycle at 900ºC for 20 minutes. The silver ink consists of a suspension of fine silver particles in a terpene oil and is available from Fuel Cell Materials. Both nickel and LSM inks are available in a similar form from the same supplier.

In order to ensure good continuity between the electrode surfaces and their respective gold meshes, nickel ink and LSM ink were then applied sparingly to their respective mesh surfaces, with any excess removed. The electrode assembly was then dried ready for use.

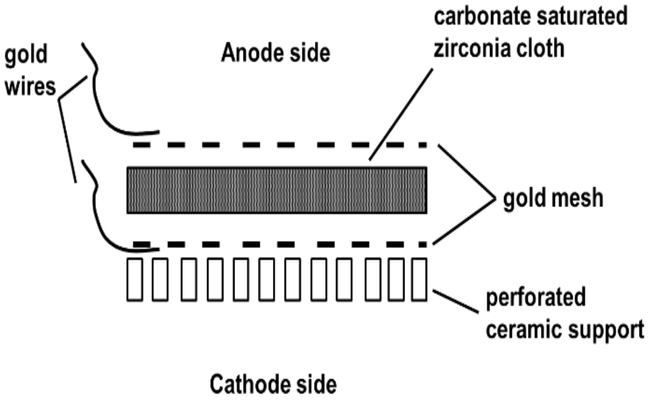

Fig. 1, MCFC electrode assemblies.

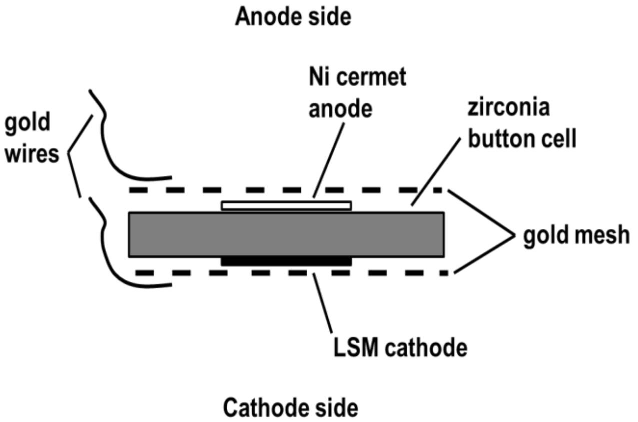

Fig. 2, SOFC electrode assemblies.

As shown in Fig. 1 and 2, gold wires (0.4 mm diameter) lead the current from the cells. These wires had flattened ends and were held in contact with the gold mesh elements by the compressive force of the external springs.

The 15 wt.% of the carbon fuel in carbonate mixture was supplied to the anode side of the cell at a fixed mass of 3.0 g for all experiments. Nitrogen gas was connected to the inlet to the anode (to purge the system from CO_2 produced) while air/CO_2 and air was supplied to the cathode chamber of the MCFC and SOFC respectively. The material supply rates used throughout are shown in Table II.

TABLE II, MATERIAL SUPPLY RATES

Fuel cell	Fuel mass (g)	Anode N_2 flow rate (l/min)	Cathode flow rate (l/min)	
			Air	CO_2
MCFC	3.0	0.2	1.5	0.6
SOFC	3.0	0.2	1.5	-

V. RESULTS AND DISCUSSION

The cell performances were monitored over a range of temperatures and those demonstrated at a fixed temperature of 800ºC are reported here. Performance is assessed in terms of voltage and power density achieved over a range of load currents, and the load currents are varied by varying the applied resistive load to the fuel cell system over the range from open circuit to 1.2 Ω. Currents are converted to current density by including the surface area of the cell anode area. Figs. 3 and 4 give the variation of cell voltage and power density with current density for the MCFC system using the three biomass chars, whilst Figs. 5 and 6 give the corresponding results for the SOFC geometry. Where mis = miscanthus, will = willow, and spr = spruce.

The voltage curves for both systems show behaviour which is consistent with that of most fuel cells, i.e. a voltage close to the predicted open circuit value at zero current, falling approximately linearly with increase in current due to Ohmic effects and followed by a more rapid fall at high currents due to mass transfer polarisation at the electrodes.

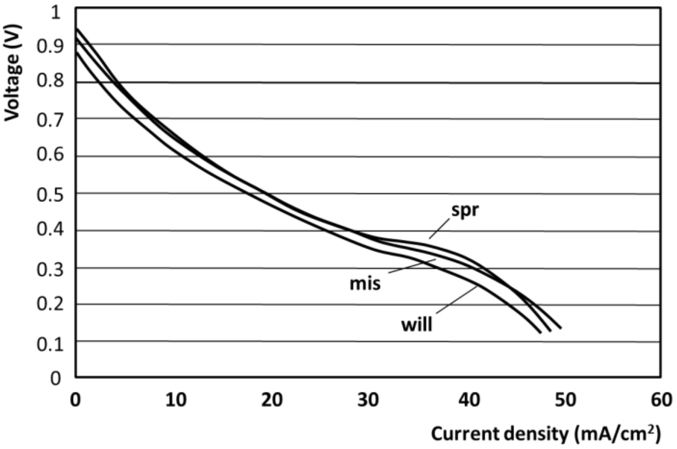

Fig. 3, Voltage vs current density for MCFC

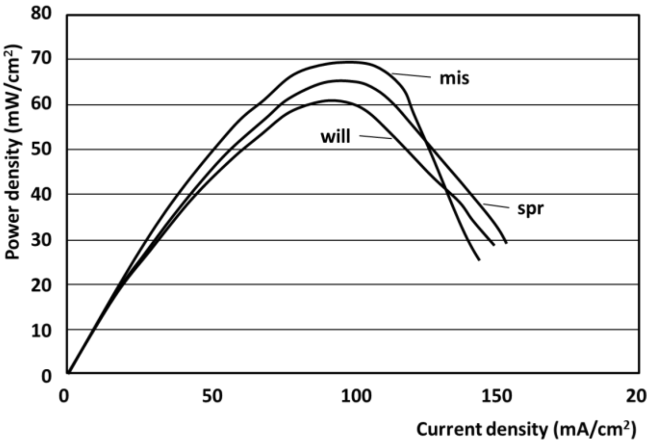

Fig. 4, Power density vs current density for MCFC

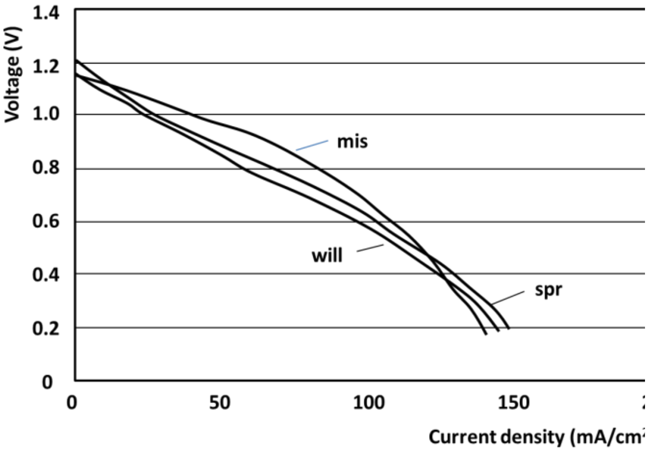

Fig. 5, Voltage vs current density for SOFC

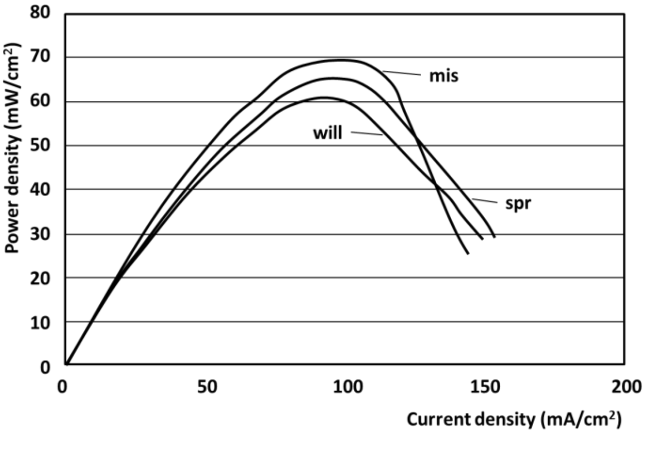

Fig. 6, Power density vs current density for SOFC

The open circuit voltage is influenced by gas species concentration and on the anode side the CO_2 concentration may be well below the O_2 value on the cathode side, particularly when gas purging is applied as in our experiments. This is predicted to raise the OCV (open circuit voltage) at zero current above the E^o (cell EMF under standard conditions) value. The measured OCV for the SOFC system was in the range of 1.15 - 1.2 V, which is consistent with other recently reported values for carbons, e.g. 1.2 V with petcoke [10] and coal [11] as carbonate fuel slurries. A lower value in the range 0.88 - 0.95 V was observed for the simpler MCFC geometry reported here. A reduction in OCV and its initial rapid fall at low currents is normally attributed to activation energy effects, and the lower value for the MCFC is attributed to the absence of any specifically chosen catalytic materials at the electrode surfaces. The more highly engineered SOFC system employs catalytic materials for both anode (Ni/cermet) and cathode (LSM), similarly to the authors reported who apply Ni and NiO [10] to the anode and cathodes respectively or who include mixed metal oxides incorporated in the fuel particles [11].

The linear sections of the the graphs in each case show closely similar gradients among the different source carbon materials indicating that their contributions to cell resistance is similar. The calculated overall values of area specific resistance ($\Delta V/\Delta I$) are 15.0 Ωcm^2 for the molten carbonate cell and 6.0 Ωcm^2 for the SOFC cell. These values reflect the effectiveness of the overall cell geometry and can be compared with recently reported values for molten hydroxide cells using coal derived fuel rods which are in the range 4.2 - 8.1 Ωcm^2 and based on areas of around 65 cm^2 [12].

The power density curves (Figs. 3-6) show a similar contrast in behaviour. These are derived as cell voltage x current density and of particular interest is the peak power density value as well as the useful range of current density, since the latter is a reflection of the overall scale of devices required to achieve an overall power level. Since the chosen operating current density will determine at which voltage level the device will be operated, the rate of voltage drop with current density will also influence the thermodynamic efficiency which can be represented by the ratio of the measured cell voltage and the theoretical OCV. It is therefore desirable that the voltage remains high as the current density rises and that the current density short circuit limit is as high as possible.

It can be seen that for the simpler MCFC, the current limit is around 50 mA/cm^2 with the peak power of 12 mW/cm^2 occurring at 30 mA/cm^2. This would be seen a being at the lower end of performance for carbon fuel cells. At the peak power level, the corresponding voltage is 0.4 V, corresponding to around 40% efficiency. Alternatively, to operate at 80% efficiency at a voltage around 0.8 V, would provide only 5 mA/cm^2. By contrast the more highly engineering SOFC system shows a current limit closer to 160 mA/cm^2, with a peak power of 70 mW/cm^2 at a current density of 100 mA/cm^2. These values arise from the better area specific ratio and higher OCV. The 80% efficiency operating level would then correspond to 75 mA/cm^2 current density.

These results using biomass chars in the SOFC geometry are generally comparable or in some cases better than the corresponding results reported for fossil fuel carbons [10–12] using a range of geometries and electrolytes and emphasises the value in considering fuel cell technology for certain components of biomass fuels in a similar way to their fossil fuel equivalents. It is clear however, that, as for fossil fuels, consideration must be given to the minimisation of cell resistance through careful choice and design of the ion transport system and catalytic enhancement of the active surfaces. The difference in results for the simple MCFC compared with the SOFC system demonstrate these points. The results have a relevance to the wider objective of identifying strategies which can be used to reduce CO_2 emissions, by exploring routes to improved electricity generation efficiency.

Biomass is widely available, and the conventional processing route to electricity has been direct burning followed by a conventional steam cycle with energy efficiencies around 35%. Gasification processes are of increasing interest for the processing of solid fuels due to the benefits of using gas turbine technology (GT) combined with steam cycles, the so-called combined cycle routes. Such combined cycle processes are capable of achieving 50%+ in energy efficiencies and the gasification process is generally favoured since the gaseous product can be fully utilised in the GT system. The conversion process to gases however, carries an energy penalty of around 30% [13], which is very much reduced if a pyrolysis process is used. However, the char fraction of such pyrolysis processes cannot be used in GT systems and its use in fuel cell systems has not yet been widely considered. The increasing interest in the use of carbons directly in fuel cells, and the repeated demonstration of high conversion efficiencies, shows that alternative combined cycles including carbon fuel cells offer the prospect of efficiency gains for biomass similar to those which have been achieved for simple fossil fuel gases via combined cycles. Data on the distribution of the primary chemical energy among the three main pyrolysis products, gas, liquid and char, are widely published [14] and pyrolysis typically yields 25 - 30wt.% solids, 10 - 20wt.% liquids with the balance as combustible gas. By exploiting the higher efficiencies available from carbon fuel cells, it therefore becomes possible to consider electricity generation via independent routes for both the solid and gas/liquid streams, the latter following a gas turbine utilisation path.

The simple comparison in Fig 7 captures the main features of such a strategy for pyrolysis routes and and a conventional biomass burning steam cycle, and combines the energy content of the processed fractions with the generation efficiency of the technology which can make use of these fractions.

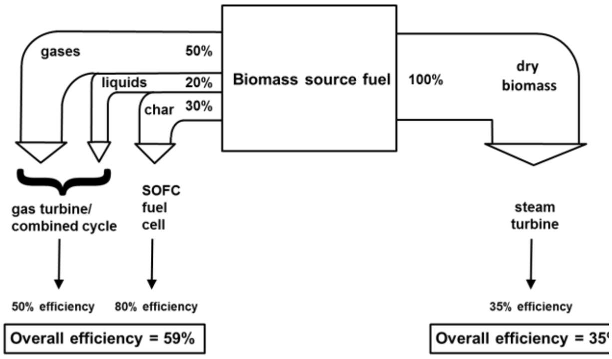

Fig. 7, Comparison of potential overall efficiencies.

As can be seen, the high efficiency of the fuel cell route for char significantly increases the overall conversion efficiency of electricity to 59% for the values chosen. The assumption here is that pyrolysis will produce around 30% char, which is a conservative figure since some reported processes achieve almost 60% char yields [9], which would further improve the overall efficiency through the fuel cell contribution.

VI. CONCLUSION

Two fuel cell designs and electrochemical performances have been reported using carbon fuel arising from the pyrolysis of commonly found biomasses. Results presented for the power density and cell voltage versus current density at 800ºC showed that peak powers of 70 mW/cm^2 at current densities of 100 mA/cm^2 were obtained using the SOFC design which was better than the MCFC design. This show that power generation from biomass using more advanced electrochemical technologies, with higher thermal efficiencies, can make a useful contribution to the overall effort to reduce CO_2 emissions. High efficiency of the fuel cell route from char significantly increases the overall conversion efficiency of electricity to 59% when compared to the conventional route of 35%.

REFERENCES

[1] D. Cao, Y. Sun and G. Wang. “Direct Carbon Fuel Cell: Fundamentals and Recent Developments,” *Journal of Power Sources*, 167(2): 250-7, 2007.

[2] R.H. Wolk, L. Scott, S. Gelber and F.H. Holcomb. “Direct carbon fuel cells: Converting waste to electricity”. *ERDC/CERL fuel cell program*, U.S. Army Corps of Engineers, Final Report, Washington D.C., Sept 2007.

[3] J.F. Cooper. “Design, efficiency and materials for carbon/air fuel cell,” *Direct Carbon fuel Cell Workshop*, Pittsburgh, PA; NETL, (US DOE Ref. UCRL-PRES-154748), July 2003.

[4] J.F. Cooper, K. Berner. “The carbon/air fuel cell, conversion of coal-derived carbons”, *The Carbon fuel Cell Seminar*, Palm Spring, CA; UCRL-PRES-216953: 1-16, November 2005.

[5] N.J. Cherepy, R. Krueger, K.J. Fiet, A.F. Jankowski and J.F. Cooper. “Direct conversion of carbon fuels in a molten carbonate fuel cell*”, J. Electrochemical Society*, 152(1) : A80-A87, 2005.

[6] S. Zecevic, E.M. Patton, and P. Parhami. “Carbon-air fuel cell without a reforming process”, *Carbon*, 42: 1983-93, 2004.

[7] H.B. Goyal, S. Diptendu, and R.C. Saxena. “Bio-fuels from thermochemical conversion of renewable resources: A review”, *Renewable & Sustainable Energy Reviews* 12:504-517, 2008.

[8] O. Onay, and O.M. Kockar. “Fixed bed pyrolysis of rapeseed (Brassica napus L.)”, *Biomass and Bioenergy*, 26:289-299, 2004.

[9] S. Sensöz. “Slow pyrolysis of wood barks from Pinus brutia Ten. and product composition”, *Bioresource Technology*, 89:307-311, 2003.

[10] L. Kouchachvili and M. Ikura. “Performance of a direct carbon fuel cell”, *Int J Hydrogen Energy*, 36:10263-10268, 2011.

[11] X. Li, Z. Zhu, R. De Marco, J. Bradley and A. Dicks. "Evaluation of raw coals as fuel for direct carbon fuel cells, *J Power Sources*, 195:4051-4058, 2010.

[12] G.A. Hackett, J.W. Zondlo and R. Svensson. "Evaluation of carbon materials for use in a direct carbon fuel cell", *J Power Sources,* 168:111-118, 2007.

[13] Y. Son, S.J. Yoon, Y.K. Kim and J-G. Lee. "Gasification and power generation characteristics of woody biomass utilizing a downdraft gasifier", *Biomass and Bioenergy,* 35:4215-4220, 2011.

[14] D.L. Klass. "*Biomass for renewable energy, fuels, and chemicals*". San Diego: Academic Press; 1998.

Journal of Energy Challenges
and Mechanics
ISSN 2056-9386
http://www.nscj.co.uk/JECM/

Scope:

Since James Watt, a Scottish inventor, improved efficiency of the steam engine, human civilization relies more and more on a steady supply of energy. Today we are at a transitional age. On the one hand, we see technology advances in the exploration and development of oil and gas, a depleting resource; we see growth in handling aging and decommissioning. On the other hand, we see ideas and plans for new energy infrastructure. This journal is about energy challenges and the underlying mechanics, involving multiple disciplines in science, technology, management and policy-making. Mechanics, fundamentally, is about force and the related behaviours, where force is about relationships, including those physical, human and social. For mechanics, the journal covers interactive boundaries with many other disciplines. For energy, topics include both fossil fuels and many different forms of renewable energy; also, issues related to energy economy, energy policy, efficiency, safety, environment and ecology will also be covered.

North Sea
Cove Bay, Aberdeen, Scotland, United Kingdom